# Computational Studies on the Dynamics of Small-Particle Suspensions using Meso-Scale Modeling

Takuya IWASHITA

2009

# Contents

# Chapter 1

# General Introduction

## 1.1 Introductory remarks

A dispersed system is defined as a heterogeneous, two-phase system in which the dispersed phase is distributed within the continuous phase. The dispersed and continuous phases are either gases, liquids, or solids. Various dispersed systems have attracted much attention in both scientific and engineering fields, such as statistical physics, soft matter physics, chemical engineering, and mechanical engineering. In our daily lives, we encounter several such dispersed systems - paints, cosmetics, inks, pastes, milk, ceramics, and slurries, for example. The classification of these dispersed systems is summarized in several ways in the next section. Three-phase flows are also encountered in engineering problems. For example, bubbles in a slurry flow result in three phases flowing together. In industrial applications such as spray drying and slurry transport, several multiphase flows exist. For the accurate control of these multiphase flows, it is important to precisely understand their dynamical behavior.

The dynamical behavior of flowing dispersed systems is very complicated. The dynamical properties have been extensively investigated in the field of rheology, which is the study of flow and deformation of materials under the influence of external forces. The study and prediction of the dynamics and rheology of dispersed systems have been subjects of both fundamental and technological interest. Although in the last decade, considerable efforts have been made to experimentally and theoretically investigate the structure and dynamics of dispersed systems, the dynamical behavior and the non-equilibrium structure are still subjects of ongoing research. Therefore, in this dissertation, we focus on the dynamical behavior of small solid particles dispersed in a Newtonian liquid. Although this dispersed system is simple compared to other systems encountered in various industrial applications, such as charged particles in electrolyte solution and solid particles in liquid crystal phases, the dynamical behavior has not been fully understood because of the complexity arising from the particle-particle and particle-fluid interactions. These systems are called suspensions.

The subject of this chapter is to provide a background in dispersed systems and to clarify the

objectives of this dissertation.

## 1.2 Classification

Dispersed systems can be classified in various ways. Classification based on the physical state of the two constituent phases is presented in Table 1.1. The dispersed phase and the dispersion medium can be either solids, liquids, or gases. Typical examples include suspensions, emulsions, and aerosols. A suspension is a solid/liquid dispersion, *e.g.*, solid particles that are dispersed in a liquid. An emulsion is a liquid/liquid dispersion in which the two phases are either completely immiscible or saturated with each other. Aerosols consist of a liquid or a solid that is dispersed in a gaseous phase.

Table 1.1: Classification Scheme of Disperse Systems on the Basis of the Physical State of the Dispersed Phase and the Dispersion Medium

| Dispersed phase | Dispersion medium | | |
|---|---|---|---|
| | Solid | Liquid | Gas |
| Solid | Solid suspension (ruby glass, opal, toothpaste) | Suspension (ink, paint, mud water, slurry) | Solid aerosol (smoke, dust) |
| Liquid | Solid emulsion (butter) | Emulsion (milk, mayonnaise, blood) | Liquid aerosol (spray, fog) |
| Gas | Solid foam (polystyrene foam) | Foam (whipped cream) | None |

Another classification scheme is based on the size of the dispersed particles in the dispersion medium. The particles of the dispersed phase may vary considerably in size, from large particles that are visible to the naked eye, to micro-scale (sub micron∼micron) particles, to particles of atomic and molecular dimensions. These dispersed systems are generally divided into three classes: molecular, colloidal, and coarse dispersions.

- Molecular dispersions are homogeneous in character and form solutions.

- Colloidal dispersions are intermediate in size, falling between solutions and coarse dispersions. The particle size of the dispersed phase ranges from $1 - 1000$ nm, and the dispersion medium is a liquid. The dispersed particles are strongly affected by thermal fluctuations due to the atomistic collisions of the surrounding liquid. The fluctuating motion of the dispersed particles is known as Brownian motion, which was first reported in 1828 by Robert Brown.

- Coarse dispersions consist of particles with sizes greater than sub-micron dimensions. The dispersed particles are unaffected by thermal fluctuations. Granular paste, in which granular powders are dispersed in a liquid, is an example of such a dispersion.

## 1.3 Suspensions

In this dissertation, the dynamical behaviors of small solid particles in Newtonian liquids, *e.g.*, suspensions, are investigated. Based on the particle size, these systems belong to the categories of colloidal and coarse dispersions. The understanding of the static and dynamical properties is a central issue in colloidal science and powder science.

Colloidal dispersions show a variety of phases depending on the volume fraction of the particles, thermal fluctuations, and the interfacial features. For nearly hard colloidal spheres that interact through a steep repulsive potential, the thermodynamic phase progresses from a colloidal fluid, to a coexistence of fluid and crystal phases, to a fully crystallized sample as the volume fraction is increased. At the highest concentrations, a colloidal glassy state is observed. On the other hand, for colloidal spheres with an attractive interaction, the destabilization of colloidal particles occurs when the repulsive force cannot counterbalance the attractive forces. Then, the aggregation of the colloidal particles is formed via the collision process of the colloidal particles. The aggregates range from highly porous structures with weak bonds between the particles, known as flocculates, to gel-like structures, known as coagulates.

The dynamical behaviors of suspensions have been extensively investigated by theory, experiments, and computer simulations. In non-equilibrium suspensions, many-body hydrodynamic interactions between the particles, mediated by the surrounding liquid, are of intrinsic importance and complicate the dynamical motions of the particles. Many suspensions show a variety of non-Newtonian behaviors, such as shear-thinning and shear-thickening. In order to determine the relationships between such non-Newtonian behaviors and the microscopic structures, an accurate understanding of the dynamical behavior of the suspensions is needed.

## 1.4 Computer simulation

Computer simulations are a very powerful tool in the investigation of dispersed systems and provide useful information about dynamical phenomena in a variety of situations. Dispersed systems, however, have a typical multi-scale problem. The molecules comprising the dispersion medium

(solvent) are smaller and move faster than the dispersed particles. The performance of a fully microscopic molecular simulation on an atomistic time scale requires a huge computational time in order to obtain physically meaningful results about the dispersed particles, for example, the diffusion coefficient of the particles. The typical time scale over which the diffusive motion takes place is very long compared to the atomistic time scale. From a computational point of view, such microscopic approaches are extremely inefficient in examining the motion of dispersed particles. In order to overcome this problem, a numerical modeling method based on a coarse-graining approach over mesoscopic scales is carried out. Mesoscopic scales, between the atomistic and macroscopic scales, are very important in dispersed systems. In such an approach, the solvent is often treated as a continuum velocity field, and this coarse-graining allows us to simulate the particle's motions at the mesoscopic scale in time and space.

On the other hand, there is another coarse-grained approach for problems related to the motion of an interface between two different phases. Examples include phase separation (vapor/liquid or liquid/liquid boundary), crystal growth (liquid/solid), and evaporation (vapor/liquid). In these systems, there exists a mesoscopic coarse-grained model based on the motion of the interface between the two phases. This model is often called the phase field model. In this model, the state of the phase is continuously represented by an order parameter. The interfacial motions can be well described by the time evolution of the order parameter. In dispersed systems, drying suspensions have a similar problem, in which the interface motions have an important role.

A coarse-graining approach based on the mesoscopic scale is considered to be effective in simulating the dynamical motion of dispersed systems.

## 1.5 Thesis objectives

In order to elucidate the dynamical behavior of suspensions, several problems were computationally investigated using the meso-scale models . These problems are as follows:

- The problem of the drying process of granular pastes.
- The problem of thermal fluctuations in colloidal dispersions.
- The problem of shear flows in colloidal dispersions.

The first problem was modeled using the phase field model. The second and third problems were modeled using the Navier-Stokes and Newtonian equations.

This dissertation is composed of seven chapters as follows:

In **Chapter 2**, the drying process of granular pastes by evaporation is studied using a numerical model. Motivated by the labyrinthine pattern experiment of Yamazaki and Mizuguchi [J. Phys. Soc. Jpn. 69 (2000) 2387], we propose the dynamics of a sweeping interface, in which the material distributed over a region is swept by a moving interface. In the model, the dispersed particles are described by a coarse-grained density field, obeying the equation of continuity. The motion of a gas/liquid interface, which occurs as a result of the evaporation, is described by a phase field model. The results of the numerical simulations are presented for one and two dimensions. The relevance of the present model to the drying experiment is discussed.

In **Chapter 3**, a newly developed numerical method for simulating colloidal dispersions is presented. We develop a numerical method that consistently implements thermal fluctuations and hydrodynamic interactions in the motion of Brownian particles dispersed in incompressible host fluids. In this method, the thermal fluctuations are introduced as random forces acting on the Brownian particles. The hydrodynamic interactions are introduced by directly resolving the fluid motions with the particle motion as a boundary condition to be satisfied. The validity of the method is carefully examined by comparing the obtained numerical results with the fluctuation−dissipation theorem, of which the analytical form is known for dispersions of a single spherical particle. Simulations are then performed for more complicated systems, such as a dispersion composed of many spherical particles and a single polymeric chain in a solvent.

In **Chapter 4**, the time scales for which our numerical model is valid are discussed in detail. In order to confirm the validity of the method, a positional correlation function of a single Brownian particle in a harmonic potential is calculated, and these results are compared with a hydrodynamic analytical solution.

In **Chapter 5**, colloidal dispersions in a simple shear flow are investigated by using a newly developed method. The short-time motion of Brownian particles in an incompressible Newtonian fluid under shear, in which the fluid inertia becomes important, is investigated by direct numerical simulation of the particulate flows. Three-dimensional simulations are performed, wherein external forces are introduced to approximately form Couette flows throughout the entire system with periodic boundary conditions. In order to examine the validity of the method, the mean square displacement of a single spherical particle in a simple shear flow is calculated, and these results are compared with a hydrodynamic analytical solution that includes the effects of the fluid inertia.

Finally, the dynamical behavior of a monodisperse dispersion composed of repulsive spherical particles is examined on short time scales, and the shear-induced diffusion coefficients are measured for several volume fractions.

In **Chapter 6**, we investigate the rheological properties of monodisperse concentrated dispersions with repulsive spherical particles by using a DNS method, accounting for a shear flow and thermal fluctuations. We observed that the apparent shear viscosity exhibits non-Newtonian behaviors such as shear-thinning at low Peclet numbers and shear-thickening at high Peclet numbers.

As the shear rate increases, the apparent viscosity for $\Phi = 0.31$ is nearly constant when $Pe < 10$ but increases linearly when $Pe > 10$. For $\Phi \geq 0.41$, the viscosity decreases at low Peclet numbers but increases linearly when $Pe > 10$. From the viscosity versus Peclet number curves, we can obtain both the low and high limiting viscosities, and these results are in good agreement with the Krieger-Doughty relationship. The shear-thickening behavior occurs at particle Reynolds numbers $Re_p > 1$ for all volume fractions. In the thickening regions, the viscosity is proportional to the shear rate, and its slope increases monotonically with increasing volume fraction. The shear-thinning of the apparent shear viscosity is caused mainly by the decrease in the direct interparticle contribution. The inertia contributions for the entire range of Peclet numbers is very small, as compared with the other contributions. As the volume fraction increases, the behavior of the MSD in the vorticity direction deviates from the analytical solution for a single Brownian particle in a shear flow. For $\Phi = 0.56$, a glassy state was observed. The diffusion coefficient for the high volume fraction has a greater increase than that of the low volume fraction with increasing Peclet number. For all volume fractions, the diffusion coefficient begins to increase linearly at $Re_p \sim 1$.

In **Chapter 7**, the thesis is summarized.

# Chapter 2

# Phase Field Model for Dynamics of Sweeping Interface

## 2.1 Introduction

Yamazaki and Mizuguchi[1] have shown that fascinating labyrinthine patterns are formed by simply drying a mixture of water and corn starch powder in the two dimensional space by two parallel glass plates; during the drying process, the powder is trapped at the interface due to surface tension and is swept away, but the interface becomes corrugated and leaves intricate patterns of powder behind. This process poses a new type of interface dynamics, which we coined term *sweeping interface dynamics*; as the interface passes over the space where some material, *e.g.*, the powder in the above experiment, is distributed, it sweeps and collects the material along itself. If the accumulated material resists being moved due to friction or some other mechanisms, the part of the interface where the material density is larger than that of neighboring parts falls behind, and consequently more material is swept into this part of the interface from the neighboring regions. This process causes the instability of the flat interface.

In this chapter, in order to study the dynamics of a sweeping interface, we construct a model based on a phase field and examine its behavior by numerical simulations.

## 2.2 Model for the drying process of the water-granule mixture

The model consists of two field variables, the phase field $u$ and the material density $v$, in the two-dimensional space. The interface dynamics is simulated by the time-dependent Ginzburg-Landau equation for the phase field $u(x, y, t)$

$$\tau \frac{\partial u}{\partial t} = l^2 \nabla^2 u + u(1-u)\Big(u - \frac{1}{2} - b\Big), \tag{2.1}$$

with a constant $b$, $\tau$ and $l$ are the time and the length scales, respectively, which characterize the interface. Its right hand side (RHS) may be derived from the free energy potential. We take $0 < b < 1/2$, then the system has a stable phase with $u = 0$ and a metastable phase with $u = 1$, which we assign for the dry and wet phases, respectively, in the present context. It is easy to see

that Eq. (2.1) has the solution

$$u(x,y,t) = \frac{1}{2}\Big[1 + \tanh\Big(\frac{1}{\sqrt{8l}}\Big(x - \sqrt{2}b\frac{l}{\tau}t\Big)\Big)\Big], \tag{2.2}$$

which represents the flat interface between the two phases and it is advancing to expand the stable dry phase with a speed proportional to $b$.

As for the material density field $v(x,y,t)$, the total amount of material should be conserved, therefore, the density field follows the equation of continuity

$$\frac{\partial v}{\partial t} = -\nabla \cdot \boldsymbol{J}, \tag{2.3}$$

with $\boldsymbol{J}$ being the material flux.

Sweeping by the interface is represented by the material flux given by

$$\boldsymbol{J} = (A(v)\nabla u)v - D(u)\nabla v. \tag{2.4}$$

The first term on the RHS represents the flux driven by the interface and the second term is the diffusion flux. In the first term, the factor $(A(v)\nabla u)$ can be regarded as the flow speed of the material driven by the interface; the factor $\nabla u$ represents the driving intensity, and $A(v)$ is a factor proportional to the mobility of the matter. The mobility $A(v)$ should be a decreasing function because, in the region with higher density, the material has difficulty in flowing due to friction. We also introduce the diffusion only within the interface region by assuming

$$D(u) = D_0 u(1-u) \tag{2.5}$$

with a constant $D_0$. This diffusion flux was originally introduced to eliminate a small scale instability, which appears in numerical simulations without the diffusion, but it is plausible that some diffusion always exists in a real system.

In reaction to the driving force on the material, the interface slows down in the large $v$ region. This may be represented by modifying the parameter $b$ in Eq. (2.1) to a funciton of $v$.

The central part of the present model for embodying the sweeping dynamics is in the interaction between the interface in the phase field and the material density given by the first term of $\boldsymbol{J}$ in Eq. (2.4) and $b(v)$ in Eq. (2.1), but their detailed forms are rather arbitrary. The important points for the sweeping dynamics of the propagating interface are (i) the interface drives the material flux that is normal to the interface, (ii) the friction of the material resists the drive (iii) the reaction

to the drive from the material slows down the interface propagation upon increasing the material density.

We employ simple forms for $b(v)$ and $A(v)$

$$b(v) = \frac{b_0}{v/v_b + 1}, \qquad A(v) = \frac{A_0}{v/v_A + 1}, \tag{2.6}$$

with constants $b_0$, $A_0$, $v_b$, and $v_A$.

## 2.3 Results and discussions

The initial material distribution is assumed to be uniform with a constant density $v_0$, namely, $v(x, y, t = 0) = v_0$, and the simulations start with a phase field

$$u(x, y, t = 0) = \frac{1}{2}\Big[1 + \tanh\Big(\frac{1}{l}(x - x_i(y))\Big)\Big], \tag{2.7}$$

with an initial interface position $x_i(y)$. Numerical integration is performed with the spatial steps $\Delta x = \Delta y = 0.5$ and the time step $\Delta t = 0.03$, using the central differences for the spatial derivatives, and the Euler method for the time derivative in the phase field equation (2.1) and the cubic interpolated profile (CIP) method,[2,3] for the equation of continuity (2.3).

The following simulations are limited to the case of $v_A = v_b$, and we employ the unit system where $v_b$, $\tau$, and $l$ are unity. Most of simulations are performed with the parameters $A_0 = 8$, $b_0 = 0.4$, and $D_0 = 1$ with $v_0 = 0.5$, unless stated otherwise.

First, we examine the one-dimensional solution, which might be considered to be a uniform solution in the $y$ direction in two dimensions; the initial $u$ is a flat interface with constant $x_i$ in Eq. (2.7). Figure 2.1(a) shows the time development of the system in one dimension; initially, the material piles up around the interface and the peak of $v$ increases as the interface advances, but eventually the peak of $v$ becomes stationary when the interface passes around $x \approx 300$ because the material starts overflowing behind the sweeping interface. The speed of the interface slows down due to the friction as the material is accumulated, but the system eventually reaches the steady state, where the profile of $v$ is stationary. The stationary profiles for a few sets of $A_0$ and $b_0$ are shown in Fig. 2.1(b); one can see the peak of $v$ is large for large $A_0$ or for small $b_0$. In the steady propagation, the material density behind the interface is the same as the material density ahead of it even though the flux is not zero at the interface; all the material is simply displaced by a certain distance.

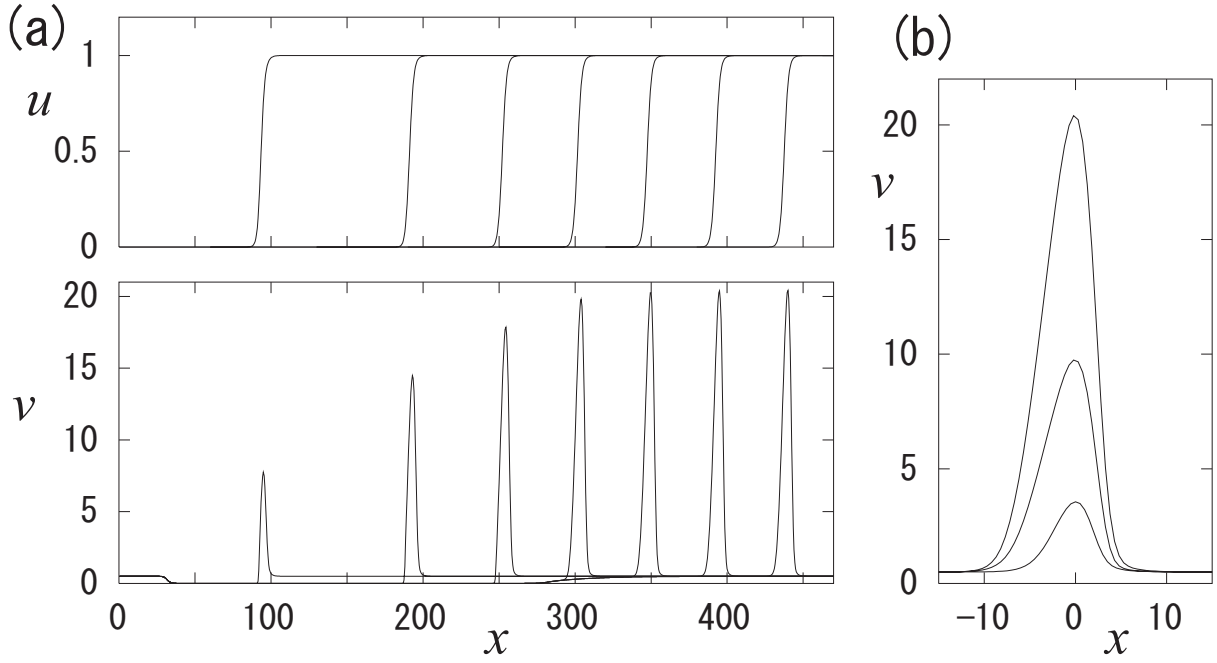


Figure 2.1: (a) Time series of 1D system. The upper and lower graphs show $u$ and $v$ fields, respectively, with the time interval of 1200. The interface is moving from left to right and the leftmost plots represent the configurations at $t = 300$. The parameters $A_0 = 8$, $b_0 = 0.4$, $D_0 = 1$, and $v_0 = 0.5$. (b) Steady profiles of material density $v$ for $(A_0, b_0) = (8, 0.4)$, $(4, 0.2)$ and $(4, 0.4)$ from top to bottom. The other parameters are $D_0 = 1$ and $v_0 = 0.5$.

The behavior without the diffusion flux in one dimension is shown in Fig. 2.2, where the profiles of $u$ and $v$ are plotted. Without the diffusion, one can see that $v$ develops a discontinuity on the rear side of the interface down to the finest spatial step introduced in numerics. We have attempted a few functional forms for $A(v)$ and $b(v)$, and different parameter values, but in all the cases, $v$ eventually develops a similar discontinuity when we uses parameter set that yields substantial accumulation.

This instability is similar to the one in the Burgers equation in the inviscid limit; on the rear side of the interface, the density $v$ is smaller than that in the preceding part. In the small $v$ region, the material flowing speed is large because $A(v)$ is large for small $v$, therefore, $v$ on the rear side is pushed forward forming a steep cliff.

Now, we study the two-dimensional system. In two dimensions, the propagation of a long straight sweeping interface is unstable; if a disturbance makes the accumulated material density at a certain part along the interface larger than that at neighboring parts, then the advancing speed of the interface becomes slower there; thus, the interface becomes concave. This makes the density $v$ increase further because the material is swept into the concave part, from which the material

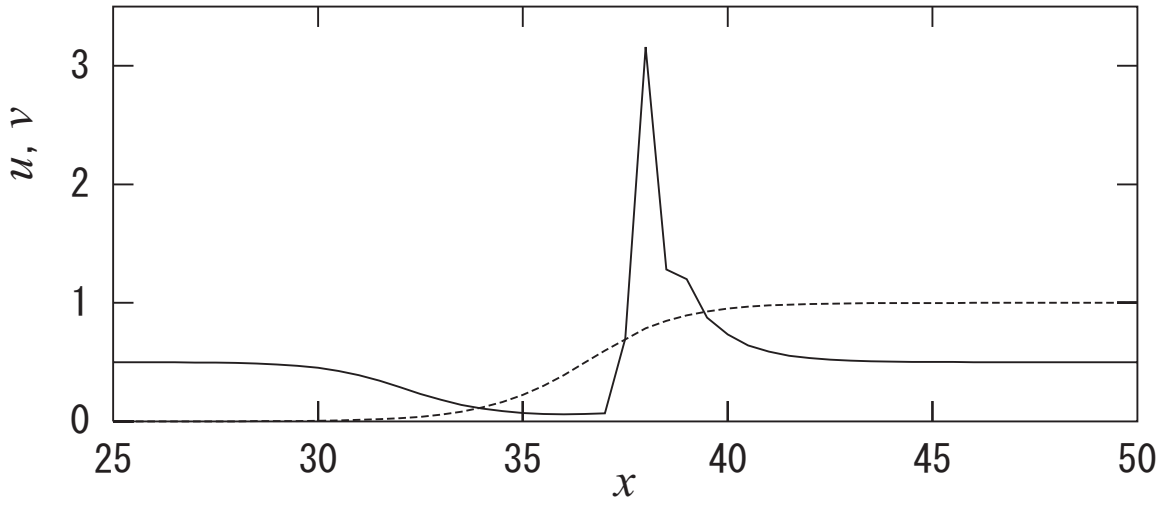


Figure 2.2: Small scale singularity in v developed in the case of $D_0 = 0$ with $A_0 = 8$, $b_0 = 0.4$, and $v_0 = 0.5$. The solid and dashed lines represent $v$ and $u$, respectively.

overflows behind the interface. This mechanism destabilizes a straight interface and results in the formation of a corrugated one, which leaves a pattern in the material after it passes.

The two-dimensional simulations are performed in the system of size $L_x \times L_y$. We employ a periodic boundary condition in the $y$ direction, but the boundaries are open in the $x$ direction.

Figure 2.3 shows the time development of the rectangular system with $L_x \times L_y = 250 \times 250$ from the initial phase field with a sinusoidally perturbed interface with the period $L_y$

$$x_i(y) \equiv x_0 + R\cos\Big(\frac{2\pi}{L_y}y\Big), \tag{2.8}$$

where $x_0$ is the initial position and $R$ is the amplitude of the perturbation; we take $x_0 = 35$ and $R = 5$ with the origin at the lower left corner. The left and right columns show the $u$ and $v$ fields, respectively. After a while, the interface develops a stationary form with a peak structure. One can see from the figure that the curved interface propagates steadily with the stationary form and it leaves a streak of the accumulated material behind the region where the interface falls behind. It should be noted that the interface in $u$ is fairly flat and does not match the line structure of $v$.

Figure 2.4 shows snapshots at $t = 1800$ for the systems with $L_x = 600$ and various widths $L_y$; the initial interface is given by Eqs. (2.7) and (2.8) with one period for each $L_y$. It shows that the curved interface becomes flat for $L_y = 15$, and the single peak interface is unstable against the formation of another peak for $L_y \gtrsim 40$. The results suggest that there is an optimal spacing for peaks in the interface. In the case of the system with $L_y = 40$, the single peak interface is unstable, and another peak tries to emerge, but cannot; the interface shows a periodic behavior.

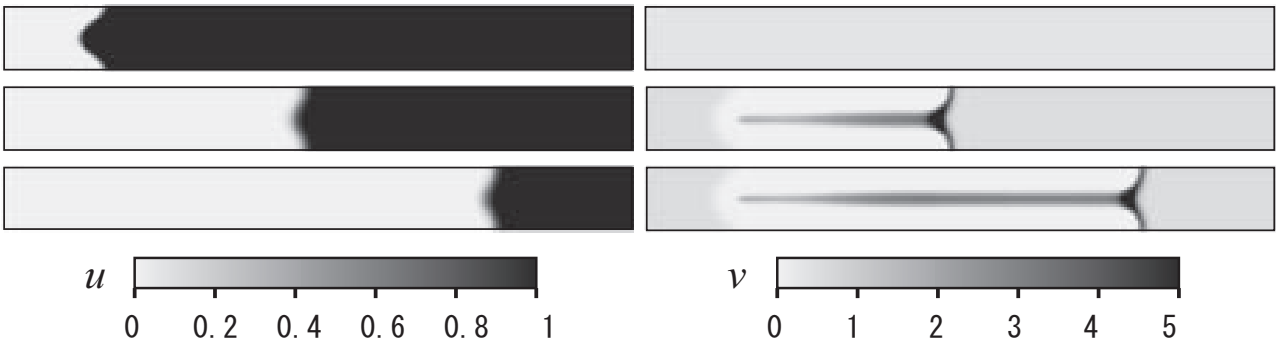


Figure 2.3: Time development of 2D system at $t = 0$, 300, and 600, from top to bottom rows. The left and right columns show $u$ and $v$, respectively. The system size is $L_x = 250$ and $L_y = 25$, and the parameters are $A_0 = 8$, $b_0 = 0.4$, $D_0 = 1$, and $v_0 = 0.5$.

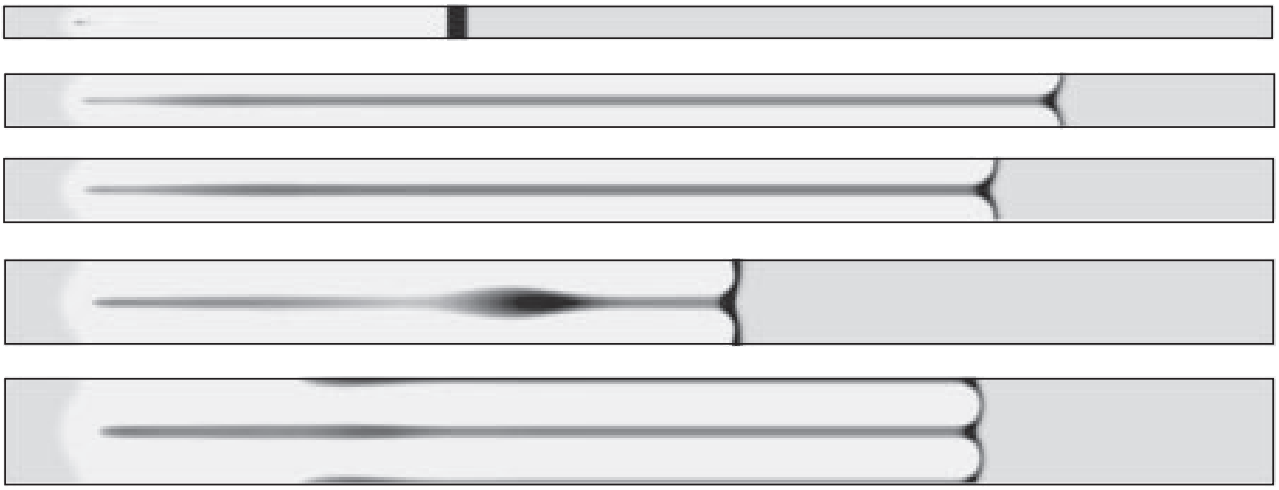

Figure 2.4: Snapshots of $v$ at $t = 1800$ for the system with $L_x = 600$ and various widths $L_y = 15$, 25, 30, 40, and 50, from top to bottom. The system length is $L_x = 600$ and the other parameters are $A_0 = 8$, $b_0 = 0.4$, $D_0 = 1$, and $v_0 = 0.5$.

Figure 2.5 shows the steady propagation speed of the interface for various systems with $L_y$. When a curved interface propagates steadily, it is much faster than the flat interface. In the curved interface, the "lighter" part with less accumulated material travels ahead and pulls up the "heavier" part, from which material drains behind more efficiently than in the case of the flat interface. The speed is slower for a wider system as long as the interface is single peaked because more material is accumulated in the concave part of the interface. For even wider systems ($L_y \gtrsim 40$), another peak appears spontaneously, and the interface speed becomes the same as that of a system of half width with a single peak interface.

The steady form of the interface changes not only with the system width $L_y$ but also with the material density $v_0$. Figure 2.6 shows the stability diagram of the curved interface with a sweeping pattern; it can be seen that the curved interface becomes flat for a large wave number $1 = L_y$

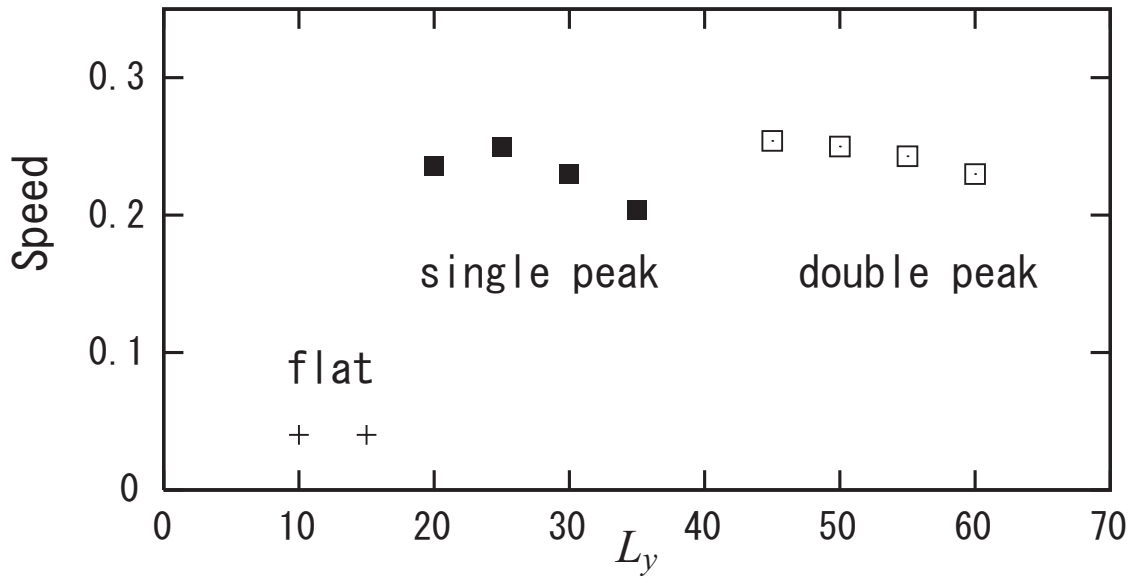


Figure 2.5: Speed of interface propagation vs. system width $L_y$. The steadily propagating interfaces are flat (pluses), single peaked (solid squares), and double peaked (open squares). The parameters are $A_0 = 8$, $b_0 = 0.4$, $D_0 = 1$, and $v_0 = 0.5$.

and/or large material density $v_0$.

This means that, for a larger density of material $v_0$, the minimum length scale of the pattern becomes larger in the present model. This is caused by interplay between the effects of friction and diffusion; for large $v_0$, the accumulation at the interface becomes large, which makes the interface motion slow, and then the distance that the material diffuses along the interface becomes large, and the length scale of the pattern becomes long.

Figure 2.7 shows a snapshot of the density field $v$ that emerges from an initial sinusoidal interface with small irregularity. The interface is initially located near the left end of the system, and at the time of the snapshot, it is located around the edge of the flat v region near the right end of the system. One can see that a small perturbation produces a globally irregular pattern. If one compares it with the patterns obtained by Yamazaki and Mizuguchi, there are both a similarity and a difference; the similarity is that any part of the region where the material is swept away is connected to the outside because the pattern is produced by the sweeping interface. The difference is that the interface remains flat over the scale that spans several streaks, and, consequently, the pattern clearly shows in which direction the interface moved, in contrast with the isotropic pattern in the experiment, where the interface is almost entirely blocked by clogging powder and corrugated wildly. It seems necessary to include a more efficient mechanism in the model to stop the interface propagation than that by the term $b$ through the function $b(v)$ in Eqs. (2.1) and (2.6).

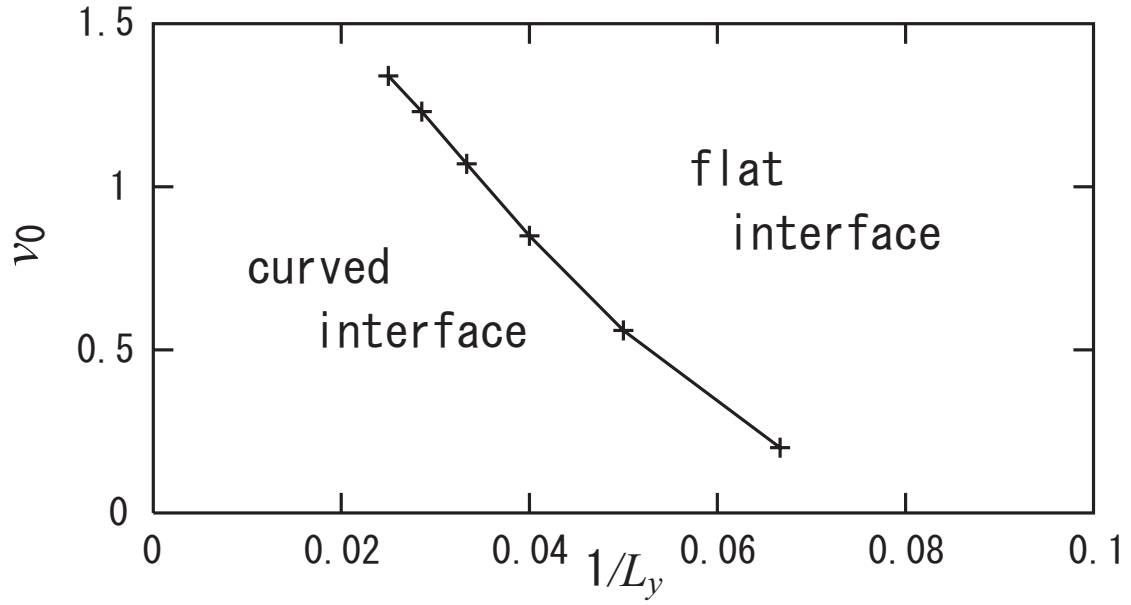


Figure 2.6: Stability diagram for the curved interface in $v_0 - 1/L_y$ plane. The parameters are $A_0 = 8$, $b_0 = 0.4$, and $D_0 = 1$.

In the experiment detailed in ref. 1, the gap between the two glass plates is determined by the size of the largest grain, namely, around 30 $\mu m$. The gap, however, can be controlled by inserting spacers. It is interesting to find that the pattern produced by the present model (Fig. 2.7) rather resembles those found in the experiments with the gap of 50 $\mu m$ or 100 $\mu m$.[4] This may be because the effect of friction is smaller for the larger gap plates.

Another difference is that, in the experiment, the scale of the pattern does not depend on the powder density, but in the present simulation, the length scale becomes large for large $v_0$ due to the diffusion, as we have seen already. Diffusion plays a subtle role in the present model. It was originally introduced to suppress a small scale singularity similar to the one in the inviscid Burgers equation, but the diffusion determines the length scale of the pattern. In this respect, we have to examine, for each $v_0$, whether there exists a small $D_0$ parameter region where the small scale singularity is suppressed, yet the global pattern is not affected by the diffusion.

In comparison with the phase field model for crystal growth,[5,6] a major difference is the length scale over which the coupling field v changes. In crystal growth dynamics, the coupling field is the temperature, and its characteristic length scale can be much larger than the interface width of the phase field. Using this length scale difference, the interface dynamics has been derived in the narrow interface limit. On the other hand, in the sweeping interface dynamics, a steep change of the coupling field $v$ seems to be intrinsic because the length scale of the variation in $v$ in the

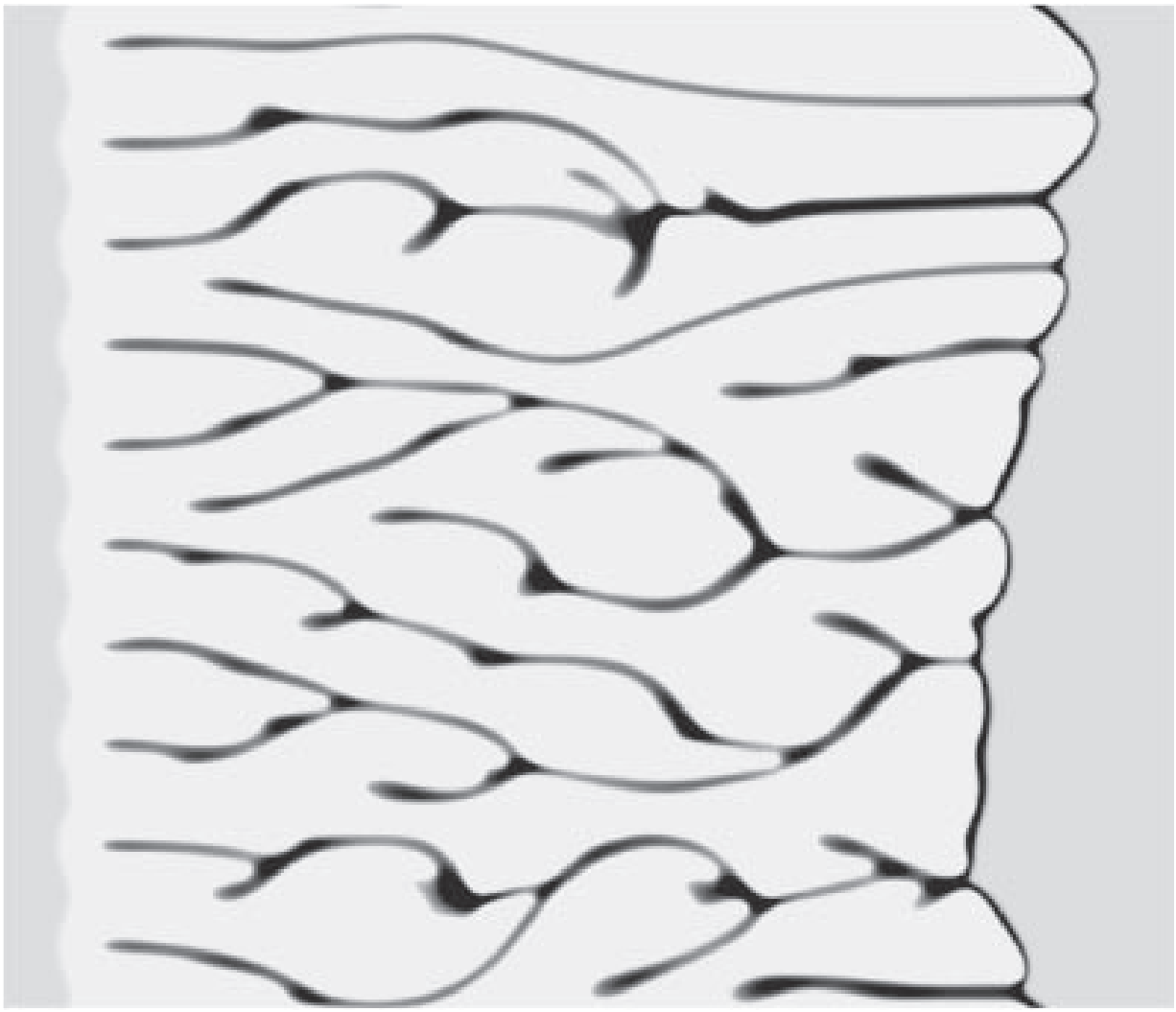

Figure 2.7: Snapshot of density $v$ from the initial interface with small irregularity. The system size is $L_x \times L_y = 700 \times 600$, and the parameters are $A_0 = 8$, $b_0 = 0.4$, and $D_0 = 1$ with $v_0 = 0.5$.

normal direction is not longer than the interface width of u even in the narrow interface limit.[7]

## 2.4 Concluding remarks

In this chapter, we have proposed the mechanism of pattern formation due to a sweeping interface and constructed a model based on the phase field. Numerical simulations were performed, which demonstrated that the flat interface becomes unstable and a pattern is produced after the interface passes.

# References


1 Y. Yamazaki and T. Mizuguchi,"Front aggregation and labyrinthine pattern in the drying Process of two-Dimensional wet granular systems", J. Phys. Soc. Jpn. **69** (2000) 2387.

2 T. Yabe, F. Xiao and T. Utsumi,"The constrained interpolation profile method for multiphase analysis", J. Comput. Phys. **169** (2001) 556.

3 T. Nakamura, R. Tanaka, T. Yabe and K. Takizawa, "Exactly conservative semi-Lagrangian scheme for multi-dimensional hyperbolic equations with directional splitting technique", J. Comput. Phys. **174** (2001) 171.

4 Y. Yamazaki, private communication.

5 R. Kobayashi, "Modeling and numerical simulations of dendritic crystal growth", Physica D **63** (1993) 410.

6 For a recent review of phase-field models, see, for example, M. Ode, S. G. Kim and T. Suzuki, "Recent Advances in the Phase-field Model for Solidification", ISIJ Int. **41** (2001) 1076.

7 G. Caginalp, "Stefan and Hele-Shaw type models as asymptotic limits of the phase-field equations", Phys. Rev. A **39** (1989) 5887.

# Chapter 3

# A Numerical Model for Brownian Particles Fluctuating in Incompressible Fluids

## 3.1 Introduction

The dynamics of solid particles dispersed in host fluids is very complicated. Although computer simulations have been extensively used as a tool to investigate those systems, obtaining meaningful results is not yet straightforward even for the simplest case where the particles are monodisperse spheres and the host fluid is Newtonian. The main difficulty comes from the consistent treatment of the so-called hydrodynamic interaction (HI) between particles mediated by fluid motions, which are induced by the particle's motion.

The mathematical expression for HI is greatly simplified if the following assumptions are made: 1) the dispersed particles are all spherical; 2) HI acting among particles is pair-wise additive; and 3) the motions of the host fluid instantaneously follows the motions of the particles (the Stokes approximation). Then, the HI is expressed as a tensor that is a function of the particle's positions and velocities, without explicitly dealing with the fluid motions. The Oseen and the Rotne-Prager-Yamakawa (RPY) tensors are probably the most well known forms of such simplified HI functions; the former neglects the size of the particle, while the latter takes into account some corrections to the particle size. The Stokesian dynamics (SD) method[1] is a widely used numerical method along the lines of solving the tensor equations. It is based on the Langevin-type equations for particles implementing the RPY tensor and the lubrication correction. The latter is necessary when the distance between particles is small compared to the particle radius.

Completely different numerical approaches have been developed recently,[2–6] where the motions of host fluids are explicitly solved along with the motion of the particles so that the HI is directly computed without using the three assumptions described above. We refer those approaches as direct numerical simulation (DNS) approaches. An apparent benefit of using DNS approaches for particle dispersions is that the long-time behavior of particle motions is reproduced accurately. For example, the velocity auto correlation function (VACF) of a fluctuating particle is expected to show a non-exponential power-law relaxation– known as the hydrodynamic long-time tail–if the thermal

fluctuations are taken into account as well.

Recently, we also proposed an efficient DNS scheme for particle dispersions called the Smoothed Profile (SP) method,[7,8] where the discontinuous boundaries between particles and a fluid are smoothed out by using a continuous profile function, thereby achieving greater computational efficiency. The SP method has been successfully applied to some problems, such as the electrophoresis of charged colloidal particles;[9] however, the effects of thermal fluctuations (TF) are neglected. This is not a bad approximation for large/heavy particles, but it is insufficient for particles whose size is on the order of a micrometer or smaller; the coupling of TF and HI becomes crucial in these systems. Owing to some new experimental techniques that enable direct examination of the properties of Brownian particles fluctuating in a host fluid, several interesting phenomena have recently been reported, including the non-diffusive behavior of Brownian particles[10] and the rotational-translation coupling of a pair of spherical particles[11] where the coupling of TF and HI plays an essential role.

In this chapter, our main goal is to implement TF and HI consistently within a DNS framework for particle dispersions. We aim to introduce TF to our original SP method to achieve this end. Since theoretical analyses have been well established for dilute dispersions, we first perform simulations for a dilute dispersion composed of a single spherical particle in a cubic box with the periodic boundary condition. The numerical results for the VACF are then compared with analytical solutions based on the fluctuation-dissipation theorem. After the validity of the method has been confirmed for this simple system, simulations are performed for dense dispersions composed of many spherical particles for which analytical solutions are unknown. We furthermore performed DNS simulations to examine the dynamics of a single polymeric chain fluctuating in a good solvent. The time-correlation functions are calculated for each Rouse mode of the chain and compared with the predictions of the Rouse and Zimm models.

## 3.2 Simulation Method

We now present our implementation of TF based on the Langevin type approach. The equation governing the solvent with a density $\rho_f$ and a shear viscosity $\eta$ is a modified Navier-Stokes equation

$$\rho_f(\partial_t \boldsymbol{v} + \boldsymbol{v} \cdot \nabla \boldsymbol{v}) = -\nabla p + \eta \nabla^2 \boldsymbol{v} + \rho_f \phi \boldsymbol{f}_p \tag{3.1}$$

with the incompressible condition $\nabla \cdot \boldsymbol{v} = 0$, where $\boldsymbol{v}(\boldsymbol{x}, t), p(\boldsymbol{x}, t)$ is the velocity and pressure field of the solvent. A smooth profile function $0 \leq \phi(\boldsymbol{x}, t) \leq 1$ distinguishes between fluid and particle

domains, namely $\phi = 1$ in the particle domain and $\phi = 0$ in the fluid domain. Those domains are separated by thin interfacial regions whose thickness is characterized by $\xi$. The body force $\phi \boldsymbol{f}_p$ is introduced to ensures the rigidity of particles and the non-slip appropriate boundary condition at the fluid/particle interface. The mathematical expressions of $\phi$ and $\phi \boldsymbol{f}_p$ are given in earlier papers[7,8] in detail.

We consider dispersions composed of $N_p$ spherical particles with a radius $a$. The motion of the $i$th particle is governed by Newton's equations of motion with stochastic forces:

$$M_i \dot{\boldsymbol{V}}_i = \boldsymbol{F}_i^H + \boldsymbol{F}_i^C + \boldsymbol{G}_i^V, \quad \dot{\boldsymbol{R}}_i = \boldsymbol{V}_i, \tag{3.2}$$

$$\boldsymbol{I}_i \cdot \dot{\boldsymbol{\Omega}}_i = \boldsymbol{N}_i^H + \boldsymbol{G}_i^\Omega, \tag{3.3}$$

where $\boldsymbol{R}_i$, $\boldsymbol{V}_i$, and $\boldsymbol{\Omega}_i$ are the position, translational velocity, and rotational velocity of particles, respectively. $M_i$ and $\boldsymbol{I}_i$ are the mass and the moment of inertia, and $\boldsymbol{F}_i^H$ and $\boldsymbol{N}_i^H$ are the hydrodynamic force and torque exerted by solvent on the particle.[7,8] $\boldsymbol{F}_i^C$ is direct interparticle interaction such as Coulombic or the Lennard-Jones potential. In the present study, we used the truncated Lennard-Jones interaction:

$$U_{LJ}(r_{ij}) = \begin{cases} 4\epsilon\left[\left(\frac{\sigma}{r_{ij}}\right)^{12} - \left(\frac{\sigma}{r_{ij}}\right)^{6}\right] + \epsilon & (r_{ij} < 2^{1/6}\sigma), \\ 0 & (r_{ij} > 2^{1/6}\sigma) \end{cases} \tag{3.4}$$

where $r_{ij} = |\boldsymbol{R}_i - \boldsymbol{R}_j|$. The parameter $\epsilon$ characterizes the strength of interactions, and $\sigma = 2a$ represents the diameter of particles. $\boldsymbol{G}_i^V$ and $\boldsymbol{G}_i^\Omega$ are random forces and torques due to thermal fluctuations, which has the following properties

$$\langle \boldsymbol{G}_i^n(t) \rangle = 0, \quad \langle \boldsymbol{G}_i^n(t) \boldsymbol{G}_j^n(0) \rangle = \alpha^n \boldsymbol{I} \delta(t) \delta_{ij} \tag{3.5}$$

where the square brackets denote taking an average over an equilibrium ensemble. $\alpha^n$ represents the noise intensity for each degree of freedom of the translation ($n = V$) and rotation ($n = \Omega$) of the particles. Each noise intensity is controlled so that the variance of the translational and rotational velocity has a constant value; that is, $\langle \boldsymbol{V}_i^2 \rangle = C_1$ and $\langle \boldsymbol{\Omega}_i^2 \rangle = C_2$, where $C_1$ and $C_2$ are constant numbers. The time evolution of the noise intensity is described by $\alpha^V(t + \Delta t) = \alpha^V(t) e^{1 - \boldsymbol{V}_i^2(t)/C_1}$ and $\alpha^\Omega(t + \Delta t) = \alpha^\Omega(t) e^{1 - \boldsymbol{\Omega}_i^2(t)/C_2}$, where $\Delta t$ is the discrete time interval which plays a role of thermostat.

The temperature of the system is defined by the diffusive motion of the dispersed particles. The translational particle temperature $k_B T^V$ is determined by the long-time diffusion coefficient $D^V$ of

a spherical particle in the Stokes-Einstein relation $k_B T^V = 6\pi\eta a D^V$ where $D^V$ is obtained from computer simulation. Similarly, the rotational particle temperature $k_B T^\Omega$ can be determined by the rotational diffusion coefficient $D^\Omega$.

There are several advantages to the Langevin approach compared with the fluctuating hydrodynamics approach, for which TF is introduced in the Navier-Stokes equation as stochastic stresses to be defined on $N^d$ grid points of fluid simulations. The fluctuating hydrodynamics is given by

$$\rho_f(\partial_t \boldsymbol{v} + \boldsymbol{v}\cdot\nabla\boldsymbol{v}) = -\nabla p + \eta\nabla^2\boldsymbol{v} + \nabla\cdot\boldsymbol{s} \tag{3.6}$$

where $\boldsymbol{s}$ is the stochastic stress satisfying the fluctuation-dissipation relation:[12]

$$\langle \boldsymbol{s}\rangle = \boldsymbol{0}, \tag{3.7}$$

$$\langle s_{ik}(\boldsymbol{x},t)s_{jl}(\boldsymbol{0},0)\rangle = 2k_BT\eta(\delta_{ij}\delta_{kl}+\delta_{il}\delta_{kj})\delta(\boldsymbol{x})\delta(t). \tag{3.8}$$

One important advantage is the computational efficiency: while a $N^d$ spatial grid requires generating $O(N^d)$ random numbers for the fluctuating hydrodynamics, our method requires $O(N_p)$ random numbers for a dispersion composed of $N_p(\ll N^d)$ particles. Second, if we consider the solvent as a complex fluid–with arbitrary constitutive equation–, our method has another merit: in the fluctuating hydrodynamics approach, the friction tensor for complex fluids is required, but not here. Derivations of the friction tensor for complex fluids often have theoretical difficulties, and even if the friction tensor is obtained, there may be a large computational cost.

## 3.3 Test of the Simulation Method

In order to test our simulation method, we consider the translational motion of a particle dragged with a constant external force $F_0$ in a Newtonian fluid. With the force turned on, a dragged particle and the solvent have a steady state solution: the particle has the constant velocity $u_0(= F_0/6\pi\eta a)$ along $x$-direction until $t = 0$. Then, for $t > 0$, the external force is removed and the particle and solvent relax toward a rest state due to dissipation. For $t > 0$, the equation of motion of the particle is described by

$$M_i\frac{du(t)}{dt} = -\Big[6\pi\eta a u(t) + \frac{2}{3}\pi\rho_f a^3\dot{u}(t) + 6a^2\sqrt{\pi\eta\rho_f}\int_{-\infty}^{t} ds\frac{\dot{u}(s)}{\sqrt{t-s}}\Big] \tag{3.9}$$

with the initial velocity $u_0$ at $t = 0$, where $u$ denotes the velocity in the $x$ direction of the particle. The right hand side in Eq. (3.9) denotes the time-dependent friction.[12] The first term in the right

hand side is the standard Stokes resistance. The second term represents the additional mass, which is related to the acceleration of the particle. The third term represents the memory effect, which addresses the temporal decay of the fluid's momentum. The equation is analytically solved, and the analytical form can be written as

$$\frac{du(t)}{dt} = -\frac{F_0}{M_e}\int_0^\infty \frac{dy}{\pi}\frac{\sigma_0\sqrt{y}e^{-y\frac{|t|}{\tau_B}}}{|1-y|^2+\sigma_0^2 y}, \tag{3.10}$$

where $\sigma_0 = (9\rho_f/(2\rho_p+\rho_f))^{1/2}$, $M_e = M_i + 2\pi\rho_f a^3/3$, $\rho_p$ the particle density and $\tau_B = M_i/6\pi\eta a$.

Numerical simulation has been performed in three dimensions with periodic boundary conditions. The lattice spacing $\Delta$ is taken to be the unit of length. Other units are defined so that we can set $\eta = 1$ and $\rho_f = 1$ in Eq. (6.6), namely the units of time, mass, pressure are given by $\rho_f\Delta^2/\eta$, $\rho_f\Delta^3$, and $\eta^2/\rho_f\Delta^2$, respectively. For a spherical particle, the radius $a = 5$, the thickness $\xi = 2$ and the particle density $\rho_p = 1$ was used.

In Fig.3.1, we plotted $-\dot{u}(t)/F_0$ for system size $32^3$, $64^3$ and $128^3$. The response function almost coincides with the analytical solution when the system size is larger. For the long-time region, the regression of the function shows a power-law decay $Bt^{-3/2}$ where $B = 1/12\rho_f(\pi\nu_f)^{3/2}$ and the kinematic viscosity $\nu_f = \eta/\rho_f$, which depends only on the hydrodynamic property of the solvent.

A basic relation between the relaxation response of a dragged particle and the velocity autocorrelation function of a Brownian particle is the fluctuation-dissipation theorem (FDT)[13]

$$-\frac{1}{F_0}\frac{du(t)}{dt} = \frac{\beta_V}{3}\langle \boldsymbol{V}_i(t)\cdot\boldsymbol{V}_i(0)\rangle \tag{3.11}$$

where $\langle \boldsymbol{V}_i(t)\cdot\boldsymbol{V}_i(0)\rangle/3$ is the translational velocity autocorrelation function (VACF) for a Brownian particle and $\beta_V = 1/k_BT^V$. The relation holds that the response function of a dragged particle with external force $F_0$ is equal to the VACF of a single Brownian particle in thermal equilibrium. Under the same computational conditions as the relaxation experiment, the VACF in thermal equilibrium has been calculated at the volume fraction $\Phi = 0.002$ and system size $64^3$. Figure 3.2 shows the VACF for a Brownian particle. We can calculate the long-time diffusion coefficient $D^V$ by the mean-square displacement of a Brownian particle;

$$\lim_{t\to\infty}\langle|\boldsymbol{R}_i(t)-\boldsymbol{R}_i(0)|^2\rangle = 6D^V t. \tag{3.12}$$

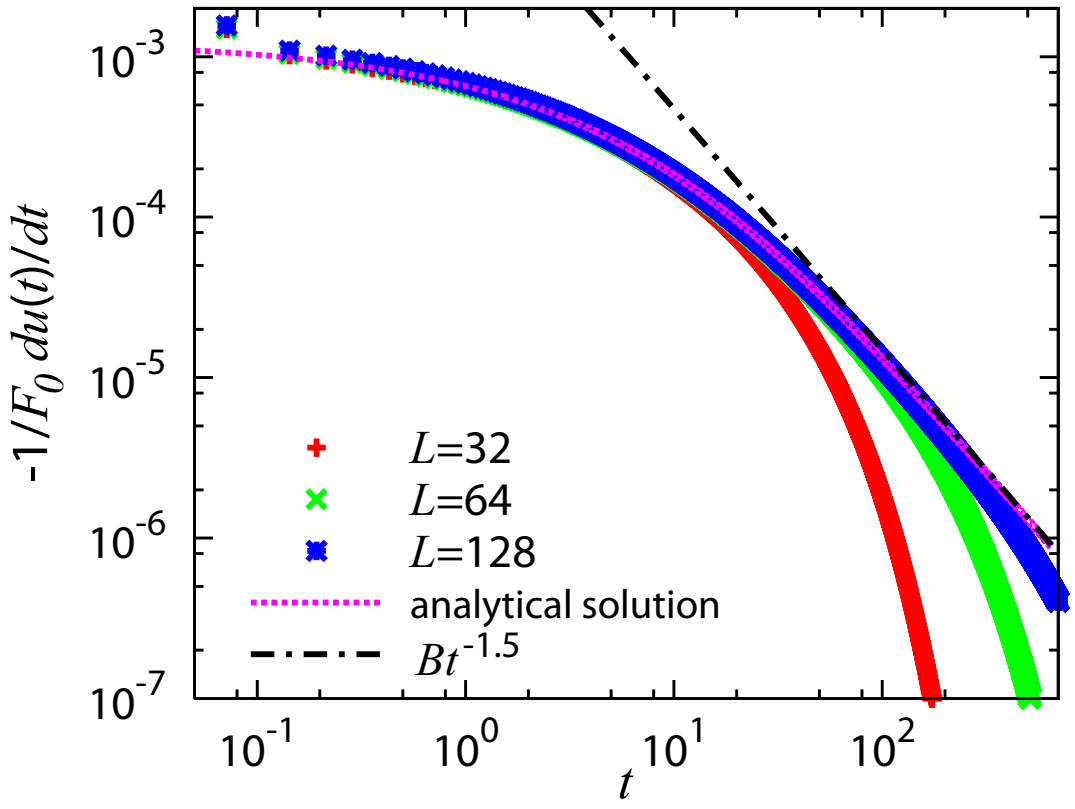


Figure 3.1: The response functions, the translational velocity of a dragged particle at a constant external force $F_0$, for system size $32^3$, $64^3$ and $128^3$. The response function is changed by the finite-size effect. Dotted line is the analytical solution of a drag problem with the time-dependent friction.[12] Dash-dotted line is the algebraic power $Bt^{-3/2}$ where $B = 1/12\rho_f(\pi\nu_f)^{3/2}$.

When simulating a Brownian particle with the HI, the diffusion coefficient is affected by finite-size effects and is given by $D^V = k_BT^V/6\pi\eta aK(\Phi)$ where $K(\Phi)$ represents the effect of the periodic boundary condition.[14,15] Taking the finite-size correction into account, the diffusion coefficient at infinite dilution is obtained as $D^V_{inf} = D^V K(\Phi)$. The translational particle temperature is estimated to be $k_BT^V = 6\pi\eta aD^V_{inf} \simeq 0.83$. In Fig.3.2, $\beta_V\langle \boldsymbol{V}_i(t)\cdot\boldsymbol{V}_i(0)\rangle/3$ approaches to the analytical solution in the long-time region, shows the power-law decay $\mathrm{B}t^{-3/2}$, and gives the response function of a dragged particle. In the short-time region, a gap between simulation and the analytical solution is observed. The amplitude of a particle's velocity is related to the equipartition law of energy; that is, $\langle \boldsymbol{V}_i^2\rangle = 3k_BT^V/M_e$ where $M_e$ denotes the effective mass. The effective mass can be obtained via a hydrodynamic calculation as $M_e = M_i + 0.5m_0$, where $m_0 = 4\pi\rho_f a^3/3$ is the mass of fluid displaced by a spherical particle with radius a. In the simulation, the effective mass is estimated to be $M_e \simeq 4.2M_i$, which is notably greater than the hydrodynamic effective mass. The disagreement may be due to the influence of the artificial smoothed boundary used between a particle and fluid.

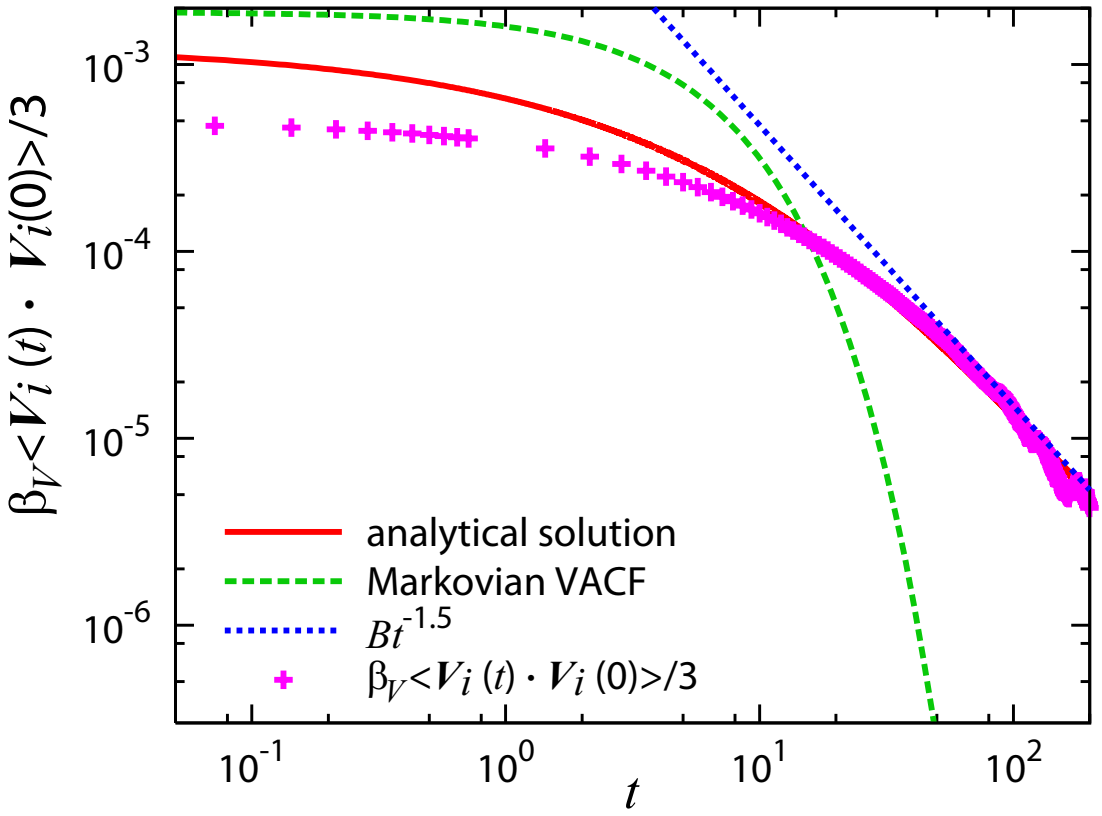


Figure 3.2: Pluses(+): Translational velocity autocorrelation function for Brownian particles at $\beta_V = 1.2$ and $\Phi = 0.002$. The solid line is the analytical solution of a drag problem for the translational particle velocity. The dotted line is the algebraic power $Bt^{-3/2}$ where $B = 1/12\rho_f(\pi\nu_f)^{3/2}$. The dashed line is the exponential decay obtained from Markovian Langevin equation, *i.e.* $M_i\dot{\boldsymbol{V}}_i = -6\pi\eta a\boldsymbol{V}_i + \boldsymbol{G}_i^V$.

In order to test the validity of the temperature estimated above of the Brownian particle, we furthermore investigate Brownian particles in harmonic potentials. The harmonic potential with a spring constant $k$ is introduced by adding $\boldsymbol{F}_i^{ex} = -k(\boldsymbol{R}_i - \boldsymbol{R}_i^{eq})$, where $\boldsymbol{R}_i^{eq}$ is its equilibrium position, to the equations of motion of particles. From statistical mechanics, the mean-square displacement of a Brownian particle trapped in a harmonic potential is given by:

$$\lim_{t\to\infty}\langle\Delta r^2(t)\rangle = \frac{2k_BT}{k}, \tag{3.13}$$

where $\langle\Delta r^2(t)\rangle = \langle|\boldsymbol{R}_i(t) - \boldsymbol{R}_i(0)|^2\rangle/3$. In the simulation for the particle number $N_p = 8$, each particle is trapped at the grids of the fcc lattice by harmonic potentials and the direct interaction between particles is ignored. For $k = 0.5, 1.0, 2.0$ and $4.0$, the $\lim_{t\to\infty}\langle\Delta r^2(t)\rangle k/2$ is plotted in Fig.3.3. The result approaches $k_BT^V$ for $k \to 0$ and is consistent with the results obtained from the diffusion coefficient for a Brownian particle.

We investigate the response function of the rotational motion of a particle with a constant

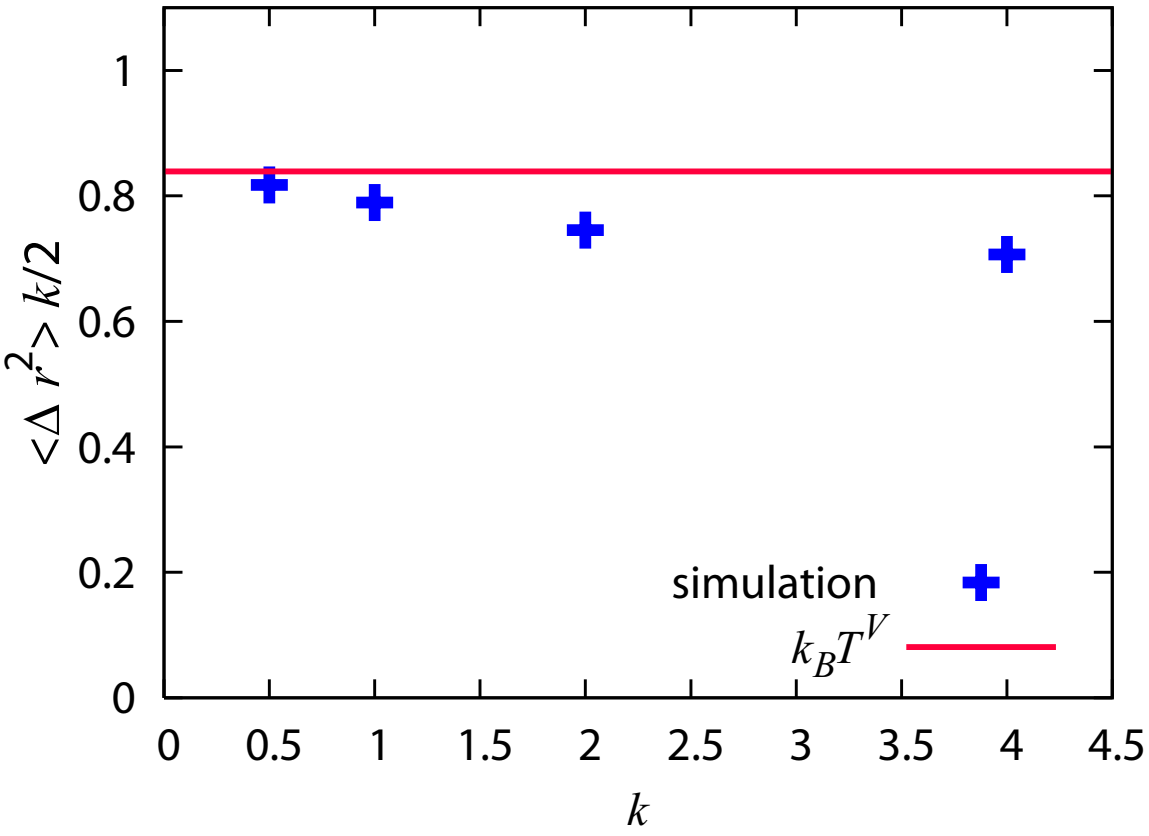


Figure 3.3: The spring constant dependence of the $\lim_{t\to\infty}\langle\Delta r^2(t)\rangle k/2$. $k_BT^V$ is the translational particle temperature, which is obtained by the diffusion coefficient for a Brownian particle.

external torque $N_0$ in a similar fashion as the investigation of the particle's translational motion. The particle has a constant rotational velocity $\omega_0(= N_0/8\pi\eta a^3)$ until $t = 0$. At $t = 0$, the imposed torque $N_0$ is removed, and for $t > 0$ the rotational motion of the particle is governed by

$$I_i\frac{d\omega}{dt} = -\int_{-\infty}^{t} ds\mu(t-s)\omega(s) \tag{3.14}$$

with the initial rotational velocity $\omega_0$ at $t = 0$, where $\omega$ denotes the rotational velocity of the particle, and the time-dependent friction $\mu(t)$ has the form $\hat{\mu}(-is) = 8\pi\eta a^3[1 - is/3\nu(1 + a\sqrt{-is/\nu})]$[16] in Fourier space. The first term in $\hat{\mu}$ is the Stokes friction, the second term represents the memory effect due to the kinematic viscosity of the fluid, and $s$ denotes numerical parameter in Fourier space. This equation is analytically solved, and the regression of the rotational velocity $\omega$ of the particle can be written as

$$\frac{d\omega(t)}{dt} = -\frac{N_0}{8\pi\eta a^3}\frac{1}{\tau_f}\int_0^\infty \frac{dy}{3\pi}\exp(-yt/\tau_f)\left[\frac{y^{3/2}}{[1-(\frac{\tau_r}{\tau_f}+\frac{1}{3})y]^2 + y(1-\frac{\tau_r}{\tau_f}y)^2}\right], \tag{3.15}$$

where $\tau_f = a^2/\nu_f$ and $\tau_r = I/8\pi\eta a^3$.

Figure 3.4 shows the relaxation response $-\dot{\omega}/N_0$. The response function almost coincides with

the analytical solution, and a power-law decay $Ct^{-5/2}$ is observed in the long-time region where $C = \pi/32\rho_f(\pi\nu_f)^{5/2}$. The FDT for the rotational velocity of a particle,

$$-\frac{1}{N_0}\frac{d\omega(t)}{dt} = \frac{\beta_\Omega}{3}\langle \boldsymbol{\Omega}_i(t)\cdot\boldsymbol{\Omega}_i(0)\rangle, \tag{3.16}$$

was also investigated. The rotational velocity autocorrelation function (RVACF) $\langle \boldsymbol{\Omega}_i(t)\cdot\boldsymbol{\Omega}_i(0)\rangle/3$ is given in Fig.3.4, where $\boldsymbol{\Omega}_i(t)$ denotes the rotational velocity of a Brownian particle. Using the Green-Kubo formula for the rotational velocity of the particle, we can obtain the rotational diffusion coefficient of the Brownian particle:

$$D^\Omega = \frac{1}{3}\int_0^\infty dt\langle \boldsymbol{\Omega}_i(t)\cdot\boldsymbol{\Omega}_i(0)\rangle. \tag{3.17}$$

Then, the diffusion coefficient is compared with the Stokes-Einstein diffusion coefficient for rotational motions, $D^\Omega = k_BT^\Omega/8\pi\eta a^3$, and the rotational particle temperature is estimated to be $k_BT^\Omega = 8\pi\eta a^3 D^\Omega \simeq 1$. The RVACF also shows a power-law decay $Ct^{-5/2}$ in the long-time region, which agrees well with Eq. (3.15). Similarly to the translational motions, the effective moment of inertia $\boldsymbol{I}_e$ can be estimated by the value of the same time correlation as $\boldsymbol{I}_e \simeq 2.6\boldsymbol{I}_i$.

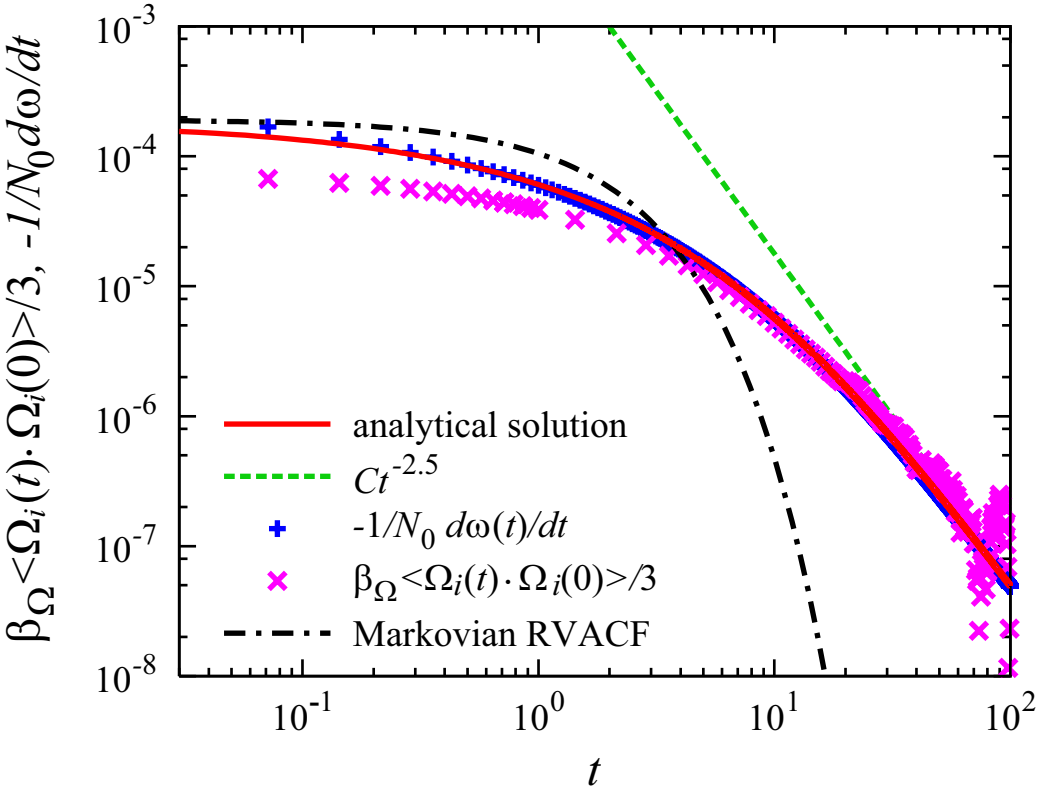


Figure 3.4: Crosses(×): Rotational velocity autocorrelation function for Brownian particles at $\beta_\Omega = 1$ and $\Phi = 0.002$. Pluses(+): The relaxation response of rotational velocity of a particle with a constant external torque $N_0$. The solid line is the analytical solution of a drag problem for the rotational particle velocity. The dashed line is the algebraic power $Ct^{-5/2}$ where $C = \pi/32\rho_f(\pi\nu_f)^{5/2}$. The dashed-dotted line is the exponential decay obtained from Markovian Langevin equation.

## 3.4 Applications

As a demonstration of a DNS incorporating thermal fluctuation of particles, our method is applied to a many-particle system and a dilute polymeric chain.

### 3.4.A Many particles system

In Fig.3.5, the translational velocity autocorrelation function for each volume fraction $\Phi$ is presented. As the volume fraction is increased, it is found that the relaxation was more rapid than in low volume fractions, and the power-law long-time tail of the VACF gradually disappear in Fig.3.5(a). Figure 3.5(b) shows that for $\Phi \geq 0.4$, the VACF has a negative overshoot, which represents an oscillative motion of a tagged particle due to a transient cage composed of surrounding particles. Compared with Brownian dynamics without HI, the decay of the correlation for a high volume fraction is much slower with HI, probably due to the lubrication force between particles.

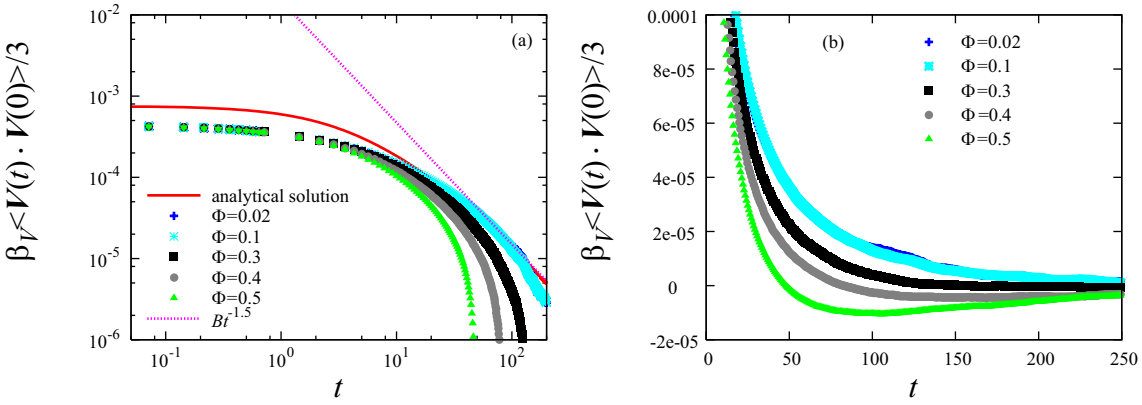


Figure 3.5: The translational velocity autocorrelation function for each volume fraction. The parameters of the simulation are $\rho_f = 1, \eta = 1, \rho_p = 1, a = 5, \xi = 2$, $\beta_V = 1$ and $\beta_\Omega = 1$. Fig.3.5(a) is the log-log plot. Fig.3.5(b) is the normal plot.

### 3.4.B A dilute polymeric chain in good solvent

The role of the HI is important in the dynamics of a dilute polymeric chain in a good solvent, and the simple theoretical model is known as the Zimm model.[17] This model treats the HI between beads as a hydrodynamic mobility matrix, such as the Oseen tensor. Some groups have studied a single polymeric chain with the HI using similar hybrid simulation methods, and their results are in agreement with the Zimm theory.[3,18,19] Here, we reexamine the validity of the Zimm model using our present DNS method since it is supposed to be more accurate than other methods used previously.

As a model of a polymeric chain, we study a bead-spring model with a truncated Lennard-Jones potential and a finitely extensible non-linear elastic (FENE) potential[20]:

$$U_F(r) = -\frac{1}{2}k_c R_0^2 \ln\{1-(r/R_0)^2\}, \tag{3.18}$$

where $k_c = 30\epsilon/\sigma^2$, $R_0 = 1.5\sigma$ and $r$ is the distance between the neighboring beads. The position vector of a bead is described by $\boldsymbol{R}_n(t)$ with $n = 0, 1, ..., N_{ch}-1$ where $N_{ch}$ denotes the total number of beads.

The static property of a polymeric chain is characterized by the static exponent $\nu$, which is defined as $\langle R_G^2 \rangle \propto N_{ch}^{2\nu} b^2$ for large $N_{ch}$, where $R_G$ is the radius of gyration and $b$ is the average bond length. The static exponent is related to the size of a polymeric chain, which is $\nu = 0.5$ for a Gaussian chain and $\nu \simeq 0.6$ for a self-avoided chain. The static exponent $\nu$ of a polymeric chain can be calculated via the static structure factor $S(k)$. Figure 3.6 displays the static structure factor for the bead numbers $N_{ch} = 10, 15$. In the range of $R_G^{-1} \ll k \ll b^{-1}$, $S(k)$ obeys the scaling relation $S(k) \propto k^{-1/\nu}$ and can determine the static exponent $\nu \sim 0.62$ by fitting a power law to our data.

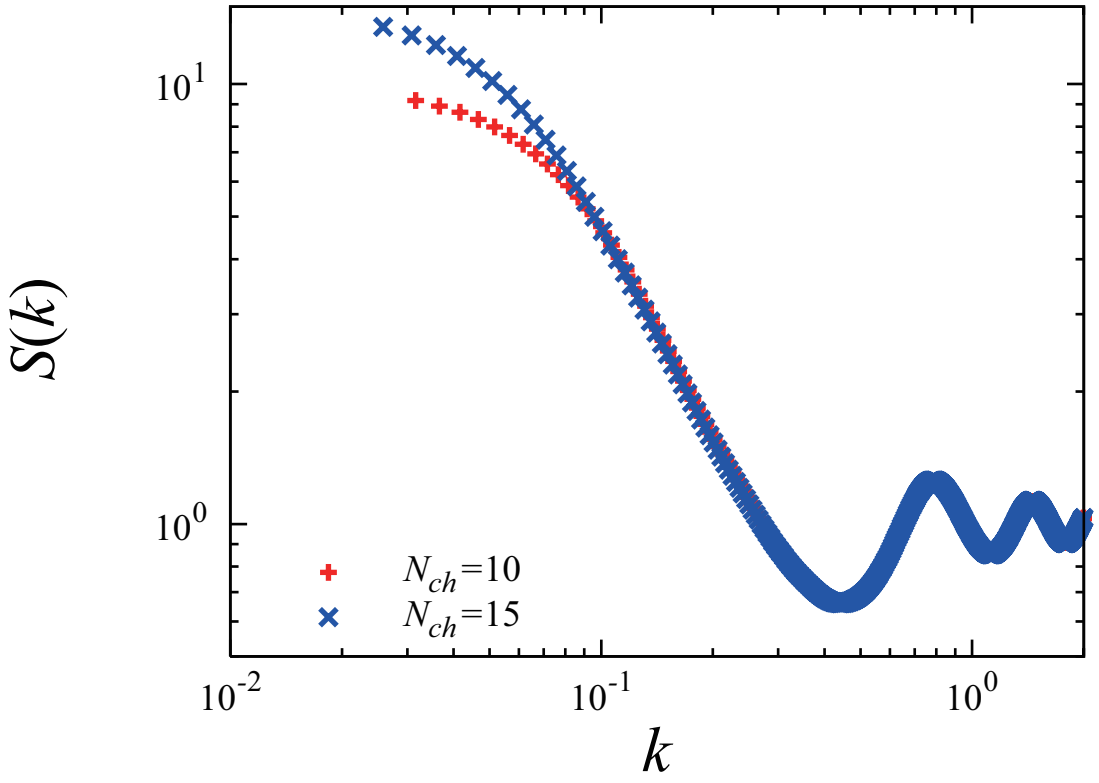


Figure 3.6: The static structure factor of a chain, for $N_{ch} = 10$ (Pluses), 15 (Crosses). The parameters of the simulation are $\rho_f = 1, \eta = 1, \rho_p = 1, a = 5, \xi = 2$, $\beta_V = 1$ and $\beta_\Omega = 1$. System size is $64^3$ grids.

To analyze the relaxation dynamics of a polymeric chain, the real space motion is decomposed

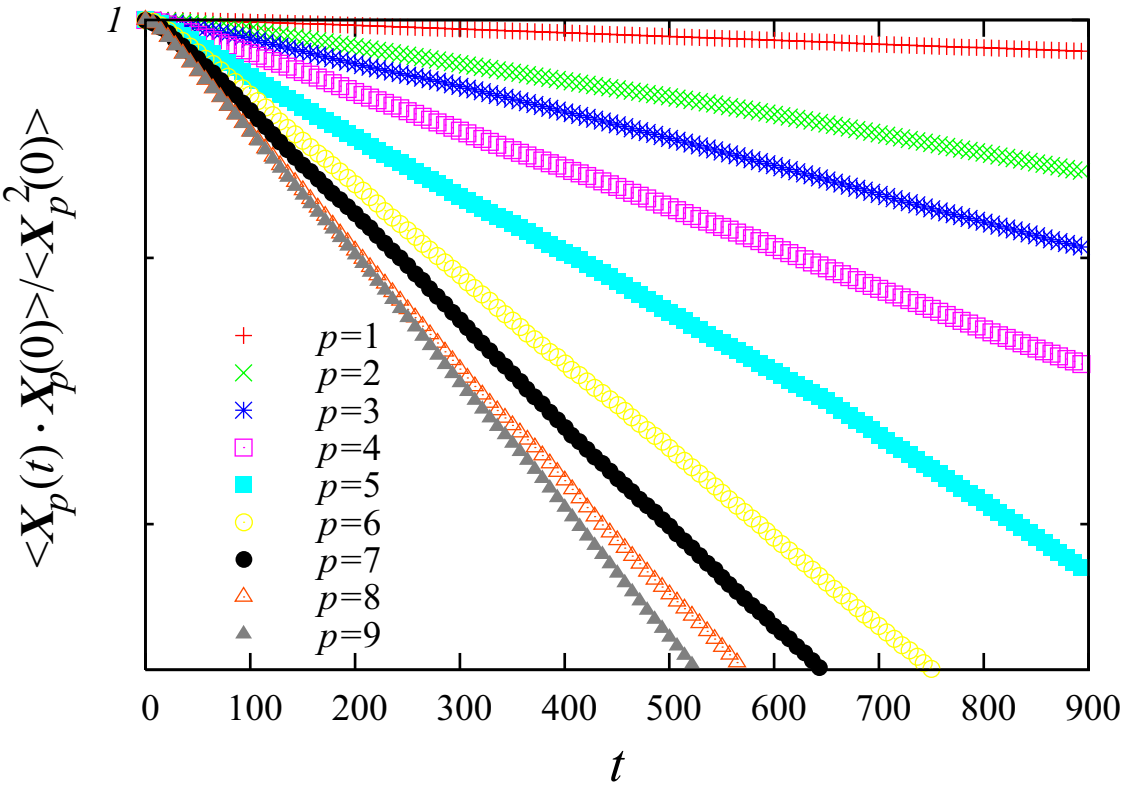


Figure 3.7: Normalized autocorrelation functions of the Rouse mode $X_p$ for various mode p. The chain length is $N_{ch} = 10$.

into a set of the Rouse modes ($p = 0, 1, \cdots, N_{ch} - 1$),

$$\boldsymbol{X}_p(t) = \frac{1}{N_{ch}} \sum_{n=1}^{N_{ch}} \boldsymbol{R}_n(t) \cos[(n - 1/2)p\pi/N_{ch}]. \tag{3.19}$$

Within the approximations of the Zimm theory, the autocorrelation function of the Rouse mode decays exponentially as $\langle \boldsymbol{X}_p(t) \cdot \boldsymbol{X}_p(0) \rangle / \langle \boldsymbol{X}_p^2 \rangle = \exp(-t/\tau_p)$, where $\tau_p$ denotes the relaxation time of the Rouse mode. The Zimm theory predicts the relation between the static exponent $\nu$ and the relaxation time $\tau_p$. The prediction is $\tau_p \sim p^{-3\nu}$ for the continuous model, and $\tau_p \sim p^{2-3\nu} \sin^{-2}(p\pi/2N_{ch})$ for the discrete model.

Figure 3.7 shows the normalized autocorrelation function of the Rouse mode for $N_{ch} = 10$. The relaxation times are obtained by a fitting in the exponential short-time regime $t \in [50 : 1000]$. Figure 3.8 shows the mode ($p$-) dependence of the relaxation time. By fitting for $p \leq 5$, the $p$-dependence of the relaxation time is estimated as $\tau_p \sim p^{-1.87}$. In Fig. 3.8, the prediction of the discrete Zimm model for the $p$-dependence of $\tau_p$ is also plotted using $\nu$ obtained from $S(k)$. The numerical results show a good agreement with the prediction of the Zimm model.

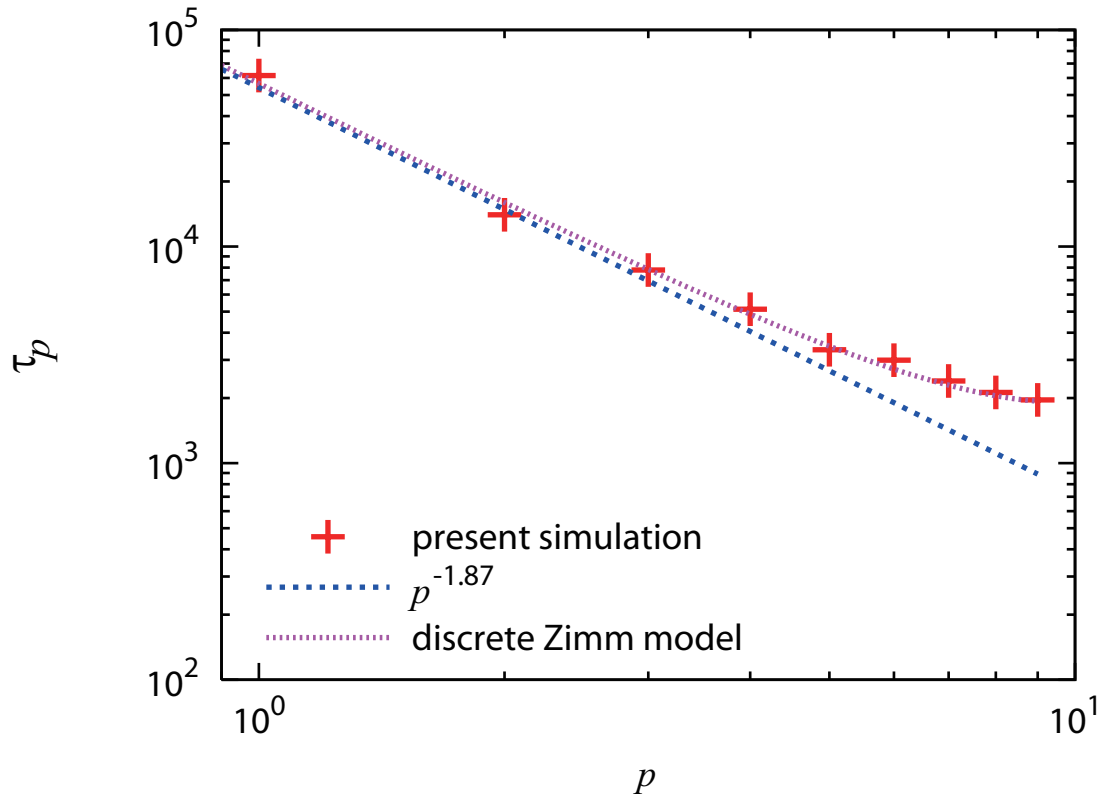


Figure 3.8: Rouse mode $p$-dependence of the relaxation time for chain length $N_{ch} = 10$. The dashed line is a fitting power law to simulation data for $p \leq 5$. The theoretical prediction of the discrete Zimm model is indicated as a dotted line, $\tau_p \sim p^{2-3\nu} \sin^{-2}(p\pi/2N_{ch})$.

## 3.5 Concluding remarks

In this chapter, we have developed a numerical method for consistently implementing thermal fluctuations and hydrodynamic interactions into models of the motions of Brownian particles dispersed in incompressible host fluids. We represented the thermal fluctuations by random forces acting on Brownian particles and the hydrodynamic interactions by directly resolving the fluid motions. The validity of the method has been examined carefully by comparing the present numerical results with the fluctuation-dissipation theorem for a dispersion of a single spherical particle. Simulations are then performed for dispersions of many spherical particles, and also for a polymeric chain in a fluid. In the former case, we found that the hydrodynamic long-time tail in the VACF–clearly observed for a single particle dispersion-becomes weak with increasing volume fraction of the particles. In the latter case, we found that our numerical results coincide quite well with the theoretical predictions of the Zimm model.

# References


1 J.F. Brady, G. Bossis, "Stokesian dynamics", Ann. Rev. Fluid Mech. **20** (1988) 111.

2 A. Malevanets and R. Kapral, "Solute molecular dynamics in a mesoscale solvent", J. Phys. Chem. **112** (2000) 7269.

3 P. Ahlrichs and B. Dünweg, "Simulation of a single polymer chain in solution by combining lattice Boltzmann and molecular dynamics", J. Phys. Chem. **111** (1999) 8225.

4 J. T. Padding and A. A. Louis, "Hydrodynamic interactions and Brownian forces in colloidal suspensions: Coarse-graining over time and length scales", Phys. Rev. E. **74** (2006) 031402.

5 P. J. Atzberger, P. R. Kramer, and C. S. Peskin, "A stochastic immersed boundary method for fluid-structure dynamics at microscopic length scales", J. Comput. Phys. **224** (2007) 1255.

6 N. Sharma and N.A. Patankar, "Direct numerical simulation of the Brownian motion of particles by using fluctuating hydrodynamic equations", J. Comput. Phys. **201** (2004) 466.

7 Y. Nakayama and R. Yamamoto, "Simulation method to resolve hydrodynamic interactions in colloidal dispersions", Phys. Rev. E. **71** (2005) 036707.

8 Y. Nakayama, K. Kim, and R. Yamamoto, "Simulating (electro)hydrodynamic effects in colloidal dispersions: smoothed profile method" Eur. Phys. J. E. (2008), 361.

9 K. Kim, Y. Nakayama, and R. Yamamoto, "Direct Numerical Simulations of Electrophoresis of Charged Colloids", Phys. Rev. Lett. **96** (2006) 208302.

10 B. Lukic, S. Jeney, C. Tischer, A. J. Kulik, L. Forro, and E. L. Florin, "Direct Observation of Nondiffusive Motion of a Brownian Particle", Phys. Rev. Lett. **95** (2005) 160601.

11 S. Martin, M. Reichert, H. Stark, and T. Gisler, "Direct Observation of Hydrodynamic Rotation-Translation Coupling between Two Colloidal Spheres", Phys. Rev. Lett. **97** (2006) 248301.

12 E. M. Lifshitz and L. D. Landau, *Fluid Mechanics,* (Addison-Wesley, Reading, 1959).

13 J. P. Hansen and I. R. Macdonald, *Theory of Simple Liquids,* (Academic press, )

14 A. A. Zick and G. M. Homsy, "Stokes flow through periodic arrays of spheres", J. Fluid Mech. **115** (1982) 13.

15 H. Hashimoto, "On the periodic fundamental solutions of the Stokes equation and their application to viscous flow past a cubic array of spheres", J. Fluid Mech. **5** (1959) 317.

16 S. H. Lamb, *Hydrodynamics,* (DOVER PUBLICATIONS, NEW YORK, 1932).

17 M. Doi and S. F. Edwards, *The Theory of Polymer Dynamics* (Oxford University Press, Oxford, 1986).

18 K. Mussawisade, M. Ripoll, R. G. Winkler, and G. Gompper, "Dynamics of polymers in a particle-based mesoscopic solvent", J. Chem. Phys **123** (2005) 144905.

19 G. Giupponi, G. De Fabritiis, and P. V. Coveney, "Hybrid method coupling fluctuating hydrodynamics and molecular dynamics for the simulation of macromolecules", J. Chem. Phys **126** (2007) 154903.

20 K. Kremer, and G. S. Grest, "Dynamics of entangled linear polymer melts: A molecular-dynamics simulationJ", Chem. Phys **92** (1990) 5057.

# Chapter 4

# Velocity autocorrelation function of fluctuating particles in incompressible fluids. - Toward direct numerical simulation of particle dispersions -

## 4.1 Introduction

The motions of small fluctuating particles in viscous fluids have been studied for a long time. Although theoretical or numerical analysis based on the coupled motions of the particles and the host fluid are very complicated, it becomes rather simple if one considers only the particles' motions by assuming that the host fluid degree of freedom can be safely projected out from the entire degree of freedom of the dispersions. One of such models is the well-known generalized Langevin equation(GLE) for Brownian particles, *i.e.*,

$$M_i \frac{d\boldsymbol{V}_i}{dt} = \int_{-\infty}^{t} ds \sum_j \Gamma_{ij}(t-s)\boldsymbol{V}_j(s) + \boldsymbol{G}_i(t), \tag{4.1}$$

$$\langle \boldsymbol{G}_i(t) \cdot \boldsymbol{G}_j(0) \rangle = 3k_B T \Gamma_{ij}(t), \tag{4.2}$$

where $M_i$ and $\boldsymbol{V}_i$ denotes the mass and the translational velocity of the $i$-th particle, respectively. $\Gamma_{ij}(t)$ is a friction tensor, which represents the effect of hydrodynamic interactions(HI) between $i$-th and $j$-th particles. $\boldsymbol{G}_i$ is the random force acting on the $i$-th particle induced by thermal fluctuations of the solvent, $k_B$ is Boltzmann constant, and $T$ is the temperature of Brownian particles.

For a single spherical particle ($i = 1$) immersed in a infinitely large host fluid, the analytic form of the time-dependent friction[1] is known as

$$\int dt \Gamma_{11}(t) \exp(-i\omega t) = \hat{\Gamma}_{11}(-i\omega) = 6\pi\eta a(1 + a\sqrt{-i\omega/\nu} - i\omega a^2/9\nu) \tag{4.3}$$

where $\hat{\Gamma_{11}}(-i\omega)$ is the Fourier transform of $\Gamma_{11}(t)$ and $\omega$ is the angular frequency. The first term corresponds to the normal Stokes friction for a spherical particle of radius $a$ in a Newtonian fluid whose viscosity is $\eta$. The second term represents the memory effect, which is related to the momentum diffusion in a viscous medium. Here the kinematic viscosity is defined as $\nu = \eta/\rho_f$ with $\rho_f$ being the density of the fluid. The third term corresponds to the effect of the acceleration of the host fluid surrounding the tagged particle when the particle is accelerated through the host fluid.

Using Eq.(4.3), the hydrodynamic GLE can be solved analytically. The translational velocity autocorrelation function (VACF) $\langle \boldsymbol{V}_i(t) \cdot \boldsymbol{V}_i(0) \rangle / 3$ was then obtained and it exhibited the characteristic power-law relaxation for long-time region, which is widely known as the "hydrodynamic long-time tail".[2–5]

For dispersions composed of many particles interacting via HI, the situation is still not straightforward because we do not know the true analytic expression for the hydrodynamic friction tensor $\Gamma_{ij}(t)$. Some approximated expressions, such as Oseen or Rotne-Prager-Yamakawa(RPY) tensor, can be obtained by introducing the Stokes approximation, however, those expressions completely neglect the memory effect that corresponds to the second term of Eq.(4.3). This means that the hydrodynamic long-time tail can not be reproduced correctly with either Oseen or RPY tensor.

In the present study, we developed a numerical method to take into account the effects of hydrodynamics directly by solving the Navier-Stokes equation for the host fluid simultaneously with the Brownian motions of the particles. We first examined the VACF for a single Brownian particle and compared the simulation results for the VACF with the analytical form mentioned above. Secondly, we examined the rotational motions of a single Brownian particle. We furthermore examined the motions of Brownian particles in harmonic potentials to check the validity of our method.

## 4.2 Simulation Method

Here we briefly explain the basic equations of our numerical model since those are explained in detail in Chapter 3. A smooth profile function $0 \leq \phi(x,t) \leq 1$ is introduced to define fluid ($\phi = 0$) and particle ($\phi = 1$) domains on a regular Cartesian grid. Those two domains are separated by thin interface regions whose thickness is $\xi$. The position of the $i$-th particle is $\boldsymbol{R}_i$, the translational velocity is $\boldsymbol{V}_i$, and the rotational velocity is $\boldsymbol{\Omega}_i$. The motion of $i$-th particle with mass $M_i$ and the moment of inertia $\boldsymbol{I}_i$ is governed by the following Langevin-type equations,

$$M_i \frac{d\boldsymbol{V}_i}{dt} = \boldsymbol{F}_i^H + \boldsymbol{F}_i^C + \boldsymbol{F}_i^{ex} + \boldsymbol{G}_i^V, \quad \frac{d\boldsymbol{R}_i}{dt} = \boldsymbol{V}_i, \tag{4.4}$$

$$\boldsymbol{I}_i \cdot \frac{d\boldsymbol{\Omega}_i}{dt} = \boldsymbol{N}_i^H + \boldsymbol{G}_i^\Omega, \tag{4.5}$$

where $\boldsymbol{F}_i^H$ and $\boldsymbol{N}_i^H$ are the hydrodynamic forces and torques acting on the $i$-th particle due to HI, respectively. $\boldsymbol{F}_i^C$ and $\boldsymbol{F}_i^{ex}$ denote the direct particle-particle interaction and external force. $\boldsymbol{G}_i^V$

and $\boldsymbol{G}_i^{\Omega}$ are the random force and torque due to thermal fluctuations defined stochastically as

$$\langle \boldsymbol{G}_i^V \rangle = \langle \boldsymbol{G}_i^{\Omega} \rangle = \boldsymbol{0}, \tag{4.6}$$

$$\langle \boldsymbol{G}_i^V(t) \cdot \boldsymbol{G}_j^V(0) \rangle = 3k_B T \alpha^V \delta(t) \delta_{ij}, \tag{4.7}$$

$$\langle \boldsymbol{G}_i^{\Omega}(t) \cdot \boldsymbol{G}_j^{\Omega}(0) \rangle = 3k_B T \alpha^{\Omega} \delta(t) \delta_{ij}, \tag{4.8}$$

where $\alpha^V$ and $\alpha^{\Omega}$ are parameters to control the temperature $T$.

The motions of the host fluid are governed by the Navier-Stokes equation

$$\rho_f(\partial_t \boldsymbol{v} + \boldsymbol{v} \cdot \nabla \boldsymbol{v}) \quad = \quad -\nabla p + \eta \nabla^2 \boldsymbol{v} + \rho_f \phi \boldsymbol{f}_p \tag{4.9}$$

with the incompressible condition $\nabla \cdot \boldsymbol{v} = 0$, where $\boldsymbol{v}$ and $p$ are the velocity and the pressure fields of the host fluid, respectively, and $\phi \boldsymbol{f}_p$ is the body force defined so that the rigidity of the particles is automatically satisfied. Note that $\boldsymbol{F}_i^H$ and $\boldsymbol{N}_i^H$ are determined from the body force $\phi \boldsymbol{f}_p$.[6,7]

## 4.3 Results and discussion

A single spherical particle fluctuating in a Newtonian fluid was simulated in the absence of external forces $\boldsymbol{F}_i^{ex} = 0$ as depicted in Fig.1. We take the mesh size $\Delta$ and $\tau = \Delta^2 \rho_f / \eta$ as the units of space and time. Simulations have been performed with $\eta = 1$, $a = 5$, and $\xi = 2$ in a three-dimensional cubic box composed of $64 \times 64 \times 64$ grid points. The particle and fluid densities are identically set to be unity, $\rho_p = \rho_f = 1$.

Figure 2 shows our simulation results ($\triangle$) of VACF for a single Brownian particle fluctuating in a Newtonian host fluid at $k_B T = 0.83$. The temperature $T$ was determined by comparing the long-time diffusion coefficient $D_{sim}$ obtained from simulations with $D^V = k_B T / 6\pi\eta a K(\Phi)$, where $K(\Phi)$ takes into account the effects of finite volume fraction[8] and $\Phi$ denotes the volume fraction. The volume fraction of a single particle is $\Phi = 0.002$. One finds that the VACF approaches asymptotically to the power-law line with the exponent $-3/2$, and the long-time behavior of our simulation agrees well with the analytical solution[5] of the hydrodynamic GLE rather than the Markovian VACF which neglects memory effects. This behavior indicates that the memory effects are accurately taken into account. Similar to the translational motions, we have studied the rotational motions of the Brownian particle in the host fluid. The GLE of the rotational motions for a single spherical

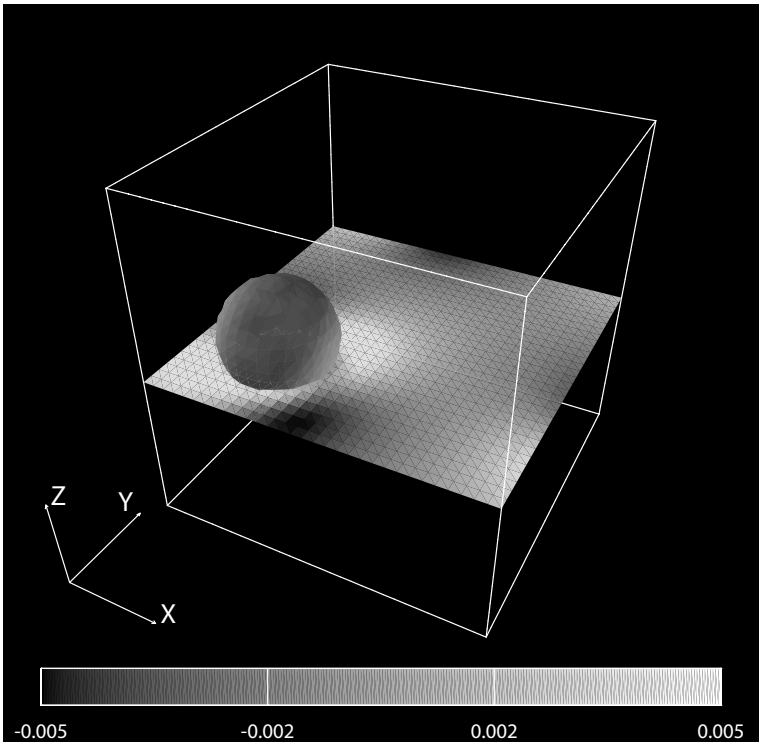


Figure 4.1: A snapshot of a single Brownian particle immersed in a Newtonian fluid. The one eighth of the entire system is graphically displayed. The color map on the horizontal plane shows the value of the local fluid velocity in the $x$ direction.

particle can be written as

$$I_i\dot{\boldsymbol{\Omega}}_i = -\int_{-\infty}^{t} ds\mu(t-s)\boldsymbol{\Omega}_i(s) + \boldsymbol{G}_i(t), \tag{4.10}$$

$$\langle \boldsymbol{G}_i \rangle = 0, \quad \langle \boldsymbol{G}_i(t)\cdot\boldsymbol{G}_i(0)\rangle = 3k_BT\mu(t), \tag{4.11}$$

where the time-dependent friction $\mu(t)$ has the form $\hat{\mu}(-i\omega) = 8\pi\eta a^3[1 - i\omega/3\nu(1 + a\sqrt{-i\omega/\nu})]$[9] in Fourier space. The first term in $\hat{\mu}$ is the Stokes friction and the second term represents the memory effect due to the kinematic viscosity of the fluid. The GLE can be solved analytically, and the analytical solution of the rotational velocity autocorrelation function (RVACF) is obtained in the following form

$$\begin{aligned}\langle \boldsymbol{\Omega}_i(t) \cdot \boldsymbol{\Omega}_i(0)\rangle \\ = -\frac{3k_BT\nu}{8\pi\eta a^5}\int_0^\infty \frac{dy}{3\pi}\exp(-yt/\tau_\nu)\left[\frac{y^{3/2}}{[1-(\frac{\tau_r}{\tau_\nu}+\frac{1}{3})y]^2 + y(1-\frac{\tau_r}{\tau_\nu}y)^2}\right],\end{aligned} \tag{4.12}$$

where $\tau_\nu = a^2/\nu$ and $\tau_r = I_i/8\pi\eta a^3$. In Fig.2, simulation results ($\bigcirc$) of RVACF are also plotted. The RVACF clearly shows the asymptotic approach to the hydrodynamic long-time tail with the exponent $-5/2$ which agrees well with the analytical solution (4.12) rather than a simple Markovian

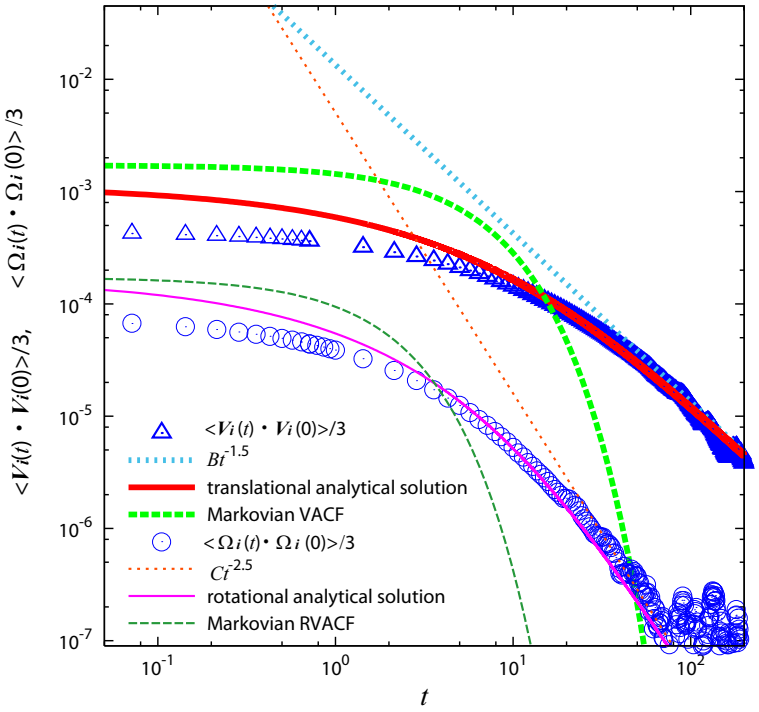


Figure 4.2: The translational velocity autocorrelation function $\langle \boldsymbol{V}_i(t) \cdot \boldsymbol{V}_i(0) \rangle / 3$ (triangle) and the rotational velocity autocorrelation function $\langle \boldsymbol{\Omega}_i(t) \cdot \boldsymbol{\Omega}_i(0) \rangle / 3$ (circle) for a single Brownian particle fluctuating in a Newtonian fluid. The simulation data was taken at $k_B T = 0.83$. The solid lines indicate the analytic results for the translational[5] and the rotational motions. The dotted lines show power-laws, $Bt^{-3/2}$ with $B = k_B T / 12 \rho_f (\pi \nu)^3$ for the translational motions and $Ct^{-5/2}$ with $C = \pi k_B T / 32 \rho_f (\pi \nu)^{5/2}$ for the rotational motions. The dashed lines indicate the Markovian VACF and RVACF, which decay exponentially as $\exp(-t/\tau_B)$ and $\exp(-t/\tau_r)$, respectively.

RVACF. By comparing the present simulation results with the corresponding analytical solutions more in detail, one may notice that some discrepancies become notable for $t < \tau_B$ or $t < \tau_r$, where $\tau_B = M_i/6\pi\eta a = 2a^2\rho_p/9\eta \simeq 5$ is the Brownian relaxation time and $\tau_r = I_i/8\pi\eta a^3 = 3\tau_B/10 \simeq 1.5$ is the Brownian rotational relaxation time. For opposite cases $t > \tau_B$ or $t > \tau_r$, however, the agreements between the numerical results and the analytical solutions are excellent. This is because we neglected memory effects in thermal noises $\boldsymbol{G}_i^V$ and $\boldsymbol{G}_i^\Omega$. We however believe that the long-time behavior of our numerical model is valid for $t > \tau_B$ since $\tau_B$ is much longer than the memory times of the thermal noises.

There exist many other characteristic time-scales in particle dispersions. Important ones are the kinematic time-scale $\tau_\nu = a^2\rho_f/\eta = 25$ which measures the momentum diffusion over the particle size and the diffusion time-scale $\tau_D = a^2/D \simeq 3 \times 10^3$ which measures the particle diffusion over the particle size. As one can see in Fig.2, the present model works quite well for the time-scales comparable to $\tau_\nu$ and $\tau_D$, while it becomes inaccurate for $t < \tau_B$.

In order to test the validity of our method for the long-time behavior of Brownian particles, we next applied the present model to simulate Brownian particles fluctuating in external harmonic potentials. The potentials are introduced with the form

$$\boldsymbol{F}_i^{ex} = -k(\boldsymbol{R}_i - \boldsymbol{R}_i^{eq}) = -k\Delta\boldsymbol{R}_i, \tag{4.13}$$

where $\boldsymbol{R}_i^{eq}$ is the $i$th particle's equilibrium position and $k$ is the spring constant.

Figure 3 shows the positional autocorrelation function $\langle\Delta\boldsymbol{R}_i(t)\cdot\Delta\boldsymbol{R}_i(0)\rangle/3$ of two Brownian particles in harmonic potentials whose minimum positions are separated by a fixed distance of $5a$. The pair of particles are interacting only hydrodynamically, and there exists no direct interactions between them. The spring constant is set to $k = 10$, and the temperature is $k_BT \simeq 0.0066$, which was determined by the average potential energy $k_BT = k\langle\Delta\boldsymbol{R}_i^2\rangle/3$. The simulation results ($\bigcirc$) agree well with the hydrodynamic analytical solution[5] in harmonic potentials which account for the effects of finite volume fraction. The analytical solution was derived by solving the GLE of a single Brownian particle in a harmonic potential which includes the modified Stokes friction $\zeta = 6\pi\eta a K(\Phi)$. The correlation functions decay much slower than the Markovian relaxation functions. We also confirmed that the validity of our method is excellent for $t \geq \tau_\nu$.

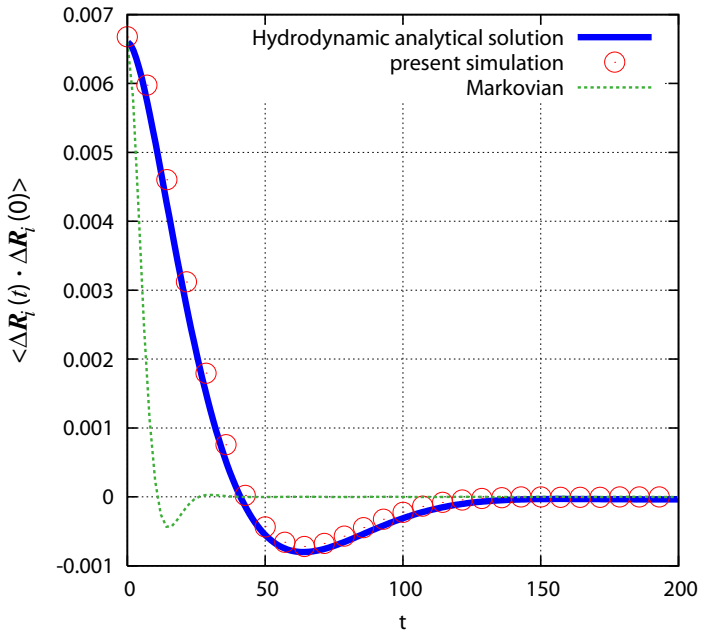


Figure 4.3: The positional autocorrelation function $\langle \Delta \boldsymbol{R}_i(t) \cdot \Delta \boldsymbol{R}_i(0) \rangle / 3$ (circle) for a system composed of two Brownian particles in harmonic potentials $-k(\boldsymbol{R}_i - \boldsymbol{R}_i^{eq})$. The distance between their equilibrium positions is $|\boldsymbol{R}_1^{eq} - \boldsymbol{R}_2^{eq}| = 5a$. The solid line shows the analytical solution.[5] The dotted line shows the Markovian functions, *i.e.* the solution of $M_i \dot{\boldsymbol{V}}_i = -6\pi\eta a \boldsymbol{V}_i - k\boldsymbol{R}_i + \boldsymbol{G}_i$.

## 4.4 Concluding remarks

In this chapter, we proposed a numerical model to simulate Brownian particles fluctuating in Newtonian host fluids, taking into account hydrodynamic interactions and thermal fluctuations. To test the validity of the model, the translational velocity autocorrelation function (VACF), the rotational velocity autocorrelation function (RVACF), and the positional autocorrelation function of fluctuating Brownian particles were calculated in some simple situations for which analytical solutions were obtained. We compared our numerical results with the analytical solutions and found excellent agreements between them specially for long-time regions $t > \tau_B$ while some discrepancies were found for short time regions $t < \tau_B$. This is because our model is designed to simulate correct long-time behaviors of Brownian particles in host fluids. Applications of the present method for more complicated situations are in progress.

# References


1 E. M. Lifshitz and L. D. Landau, *Fluid Mechanics,* (Addison-Wesley, Reading, 1959).

2 B. J. Alder and T. E. Wainwright, "Decay of the Velocity Autocorrelation Function", Phys. Rev. A. **1** (1970), 18

3 A. Widom, "Velocity Fluctuations of a Hard-Core Brownian Particle", Phys. Rev. A. **3** (1971), 1394

4 E. H. Hauge and A. Martin-Lö, "Fluctuating hydrodynamics and Brownian motion", J. Stat. Phys. **7** (1973), 259

5 H. J. H. Clercx and P. P. J. Schram,"Brownian particles in shear flow and harmonic potentials: A study of long-time tails", Phys. Rev. A. **46** (1992), 1942.

6 Y. Nakayama and R. Yamamoto, "Simulation method to resolve hydrodynamic interactions in colloidal dispersions", Phys. Rev. E. **71** (2005) 036707.

7 Y. Nakayama, K. Kim, and R. Yamamoto, "Simulating (electro)hydrodynamic effects in colloidal dispersions: smoothed profile method" Eur. Phys. J. E. (2008), 361.

8 A. A. Zick and G. M. Homsy, "Stokes flow through periodic arrays of spheres", J. Fluid Mech. **115** (1982) 13.

9 S. H. Lamb, *Hydrodynamics,* (DOVER PUBLICATIONS, NEW YORK, 1932).

# Chapter 5

# Short-time motion of Brownian particles in a shear flow

## 5.1 Introduction

The short-time motion of small particles fluctuating in a Newtonian fluid is strongly affected by fluid inertia, that is, the vorticity of the host fluid surrounding the dispersed particles. If a dispersed particle accelerates due to Brownian forces, it affects the motion of the host fluid in the neighborhood of the particle, while the vorticity generated by the particle's motion then affects the motion of the same particle. These effects are referred to as memory effects and have an important role in the dynamical motion of a dispersion on short time scales.[1–3]

The vorticity diffuses away on a kinematic time scale $\tau_\nu = a^2/\nu$, where $a$ is the radius of the spherical particle and $\nu$ is the kinematic viscosity of the host fluid ($\sim 10^{-7}$ s for 1 $\mu$m in water). When the vorticity diffuses away much faster than the particle's motion, *i.e.* $\tau_\nu \ll \tau_B = M/6\pi\eta a$ where $M$ is the mass of a Brownian particle and $\eta$ is the shear viscosity of the host fluid, the motion of a Brownian particle is well approximated by the normal Langevin equation, which is valid for strong damping (Reynolds number $Re \to 0$) or long time scales; however, this equation, wherein the effects of the fluid inertia are ignored is not applicable to a dispersion composed of neutrally buoyant particles since $\tau_B$ is comparable to $\tau_\nu$. For a complete understanding of the short-time motion of a dispersion, the inertias of the particle and the host fluid cannot be neglected.

One way to account for memory effects is to simultaneously resolve the fluid motion with the particle motion as a boundary condition to be satisfied. We refer to this approach as the direct numerical simulation(DNS) approach. Within the DNS approach, various numerical methods have been developed,[5,8,13,14,18] and the power-law decay behavior in the velocity autocorrelations of a free Brownian particle has been accurately reproduced. This slow relaxation of the correlation behavior is one of the main features of memory effects. Although most of these methods have been applied to dispersions composed of free Brownian particles at thermal equilibrium, dispersions under flows that are far from equilibrium have not been examined in detail, even for the simple case of a single Brownian particle in a shear flow on a short time scale, $\tau_\nu$. Furthermore, most numer-

ical methods used for concentrated dispersions under shear, which are widely used for measuring rheological properties, are limited to a Reynolds number of zero, and the short-time motions of the dispersed particles in concentrated dispersions cannot be correctly tracked.

Recently, we have developed a numerical method, known as the "Smoothed Particle Method(SPM)",[9,10] for the DNS of particulate flows. The SPM has been applied to a dispersion composed of free Brownian particles at thermal equilibrium in Chapter 3 and 4. We have also succeeded in reproducing the power-law decay behavior in the translational and rotational velocity autocorrelations of a Brownian particle, and these results agreed well with hydrodynamic analytical solutions for a free Brownian particle in an infinite fluid that accounts for memory effects.

In order to simulate dispersions in non-equilibrium conditions on short time scales in which memory effects become significant, we have modified the SPM. The primary objective of the present work is to accurately examine the short-time motion of Brownian particles in a simple shear flow by using the modified SPM. In this paper, we first present the modified SPM, in which external forces are introduced to impose a shear flow into the system. In order to validate the method, we next compare the numerical results for the mean square displacement (MSD) with hydrodynamic analytical solutions of a Brownian particle in a simple shear flow that account for fluid inertia. Furthermore, we apply our method to a dispersion composed of many spherical particles under shear. The MSD in the vorticity direction is then calculated for several volume fractions, and the time evolution is discussed. Finally, the shear-induced diffusion coefficients are measured from the long-time behavior of the MSD, and the dependence of the resulting diffusion coefficients on the volume fraction is examined.

## 5.2 Simulation method

Let us consider a monodisperse dispersion of repulsive spherical particles in a Newtonian host fluid. The dispersion is subjected to shear by an external force. The position of the $i$th particle is $\boldsymbol{R}_i$, the translational velocity is $\boldsymbol{V}_i$, and the rotational velocity is $\boldsymbol{\Omega}_i$. The velocity and pressure fields of the host fluid are $\boldsymbol{v}(\boldsymbol{x},t)$ and $p(\boldsymbol{x},t)$, respectively. These field quantities are defined on three-dimensional Cartesian grids; $\boldsymbol{x} \in [0,L_x][-L_y/2,L_y/2][0,L_z]$. In order to distinguish the particle and fluid domains on the grids, a smoothed function $\phi(\boldsymbol{x},t)$, which is equal to 1 in the particle domains and 0 in the fluid domains, is introduced. These domains are separated by a thin interfacial domain of thickness $\xi$. The length unit is taken to be the lattice spacing $\Delta$, and the time unit is

$\rho_f \Delta^2/\eta$, where $\rho_f$ denotes the density of the host fluid. The time evolution of the $i$th dispersed particle with mass $M_i$ and moment of inertia $\boldsymbol{I}_i$ is governed by Newton's equations of motion:

$$M_i \dot{\boldsymbol{V}}_i = \boldsymbol{F}_i^H + \boldsymbol{F}_i^C + \boldsymbol{G}_i^V, \quad \dot{\boldsymbol{R}}_i = \boldsymbol{V}_i, \tag{5.1}$$

$$\boldsymbol{I}_i \cdot \dot{\boldsymbol{\Omega}}_i = \boldsymbol{N}_i^H + \boldsymbol{G}_i^\Omega, \tag{5.2}$$

where $\boldsymbol{F}_i^H$ and $\boldsymbol{N}_i^H$ are the hydrodynamic forces and torques exerted by the host fluid on the particle.[9,10] $\boldsymbol{F}_i^C$ is a repulsive force that is employed to prevent particle overlaps, and a truncated Lennard-Jones potential, $V(r_{ij}) = 4[(\sigma/r_{ij})^{36} - (\sigma/r_{ij})^{18} + 1/4]$ for $r_{ij} < 2^{1/18}\sigma$ or $V(r_{ij}) = 0$, is adopted in this work. Here $r_{ij} = |\boldsymbol{R}_i - \boldsymbol{R}_j|$, and $\sigma = 2a$ represents the diameter of particles. $\boldsymbol{G}_i^V$ and $\boldsymbol{G}_i^\Omega$ are random forces and torques, respectively, due to thermal fluctuations. These fluctuations are introduced as white noise with a zero mean and correlations $\langle \boldsymbol{G}_i^V(t)\boldsymbol{G}_j^V(0)\rangle = k_B T^V \alpha^V \boldsymbol{I}\delta(t)\delta_{ij}$ and $\langle \boldsymbol{G}_i^\Omega(t)\boldsymbol{G}_j^\Omega(0)\rangle = k_B T^\Omega \alpha^\Omega \boldsymbol{I}\delta(t)\delta_{ij}$, where $\alpha^V$ and $\alpha^\Omega$ are numerical parameters that control the translational and rotational particle temperatures, namely, $T^V$ and $T^\Omega$. The angular brackets denote taking an average over an equilibrium ensemble. The temperatures are determined by the following procedure; First a single Brownian particle at equilibrium is simulated with fixed $\alpha_V$ and $\alpha_\Omega$. Then the translational and rotational long-time diffusion coefficients are obtained from the simulation. By comparing these diffusion coefficients with Stokes-Einstein diffusion coefficients, $D_0^V = k_B T^V/6\pi\eta a$ for the translational motion and $D_0^\Omega = k_B T^\Omega/8\pi\eta a^3$ for the rotational motion, we finally can determine the temperatures. Since both $\alpha_V$ and $\alpha_\Omega$ are chosen to satisfy $k_B T^V = k_B T^\Omega$, the temperatures are simply written as $k_B T$ throughout this paper.

The time evolution of the host fluid is governed by the Navier-Stokes equations:

$$\rho_f(\partial_t \boldsymbol{v} + \boldsymbol{v}\cdot\nabla\boldsymbol{v}) = \nabla\cdot\boldsymbol{\sigma} + \rho_f\phi\boldsymbol{f}_p + \rho_f\boldsymbol{f}^{shear}, \tag{5.3}$$

$$\boldsymbol{\sigma} = -p\boldsymbol{I} + \eta\{\nabla\boldsymbol{v} + (\nabla\boldsymbol{v})^T\} \tag{5.4}$$

where the incompressibility condition, $\nabla\cdot\boldsymbol{v} = 0$. $\boldsymbol{f}^{shear}(\boldsymbol{x},t)$ is an external force field that is introduced to enforce the following velocity profile,

$$v_x(y) = \begin{cases} \dot\gamma(-y - L_y/2), & (-L_y/2 < y \le -L_y/4) \\ \dot\gamma y, & (-L_y/4 < y \le L_y/4) \\ \dot\gamma(-y + L_y/2) & (L_y/4 < y \le L_y/2) \end{cases} \tag{5.5}$$

where $\dot\gamma$ denotes the shear rate of the imposed flow and $y$ denotes the distance in the velocity-gradient direction. This velocity profile, schematically depicted in Fig. 5.1, enables us to solve the

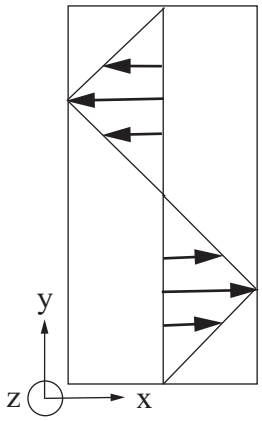


Figure 5.1: Schematic diagrams of a zigzag velocity flow. The arrows represent the velocity vectors of the host fluid in the flow direction. The $x$, $y$, and $z$ axis represent the flow, velocity-gradient, and vorticity directions, respectively

motion of the host fluid with periodic boundary conditions. Couette flow profiles are approximately formed over a range from $y = -L_y/4$ to $y = L_y/4$, although the zigzag profile strictly becomes a Couette flow when $L_y \to \infty$. $\phi \boldsymbol{f}_p$ represents the body force that ensures the rigidity of particles and the aprropriate non-slip boundary conditions at the fluid/particle interface, which is further elaborated in reference.[9,10]

## 5.3 Results and Discussion

The computational domain has three dimensions $64 \times 64 \times 64$ and periodic boundary conditions. The numerical parameters for both the host fluid and the spherical particles are $\Delta = 1$, $\eta = 1$, $\rho_f = 1$, $a = 5$, $\xi = 2$, and particle density $\rho_p = 1$. The imposed shear rate is $\dot{\gamma} = 0.005$, and the temperature is $k_B T = 0.07$. The temperature was determined by measuring the long-time diffusion coefficient of a single Brownian particle at equilibrium before the shear was imposed. This system has dimensionless parameters such that the Peclet number $Pe = 6\pi\eta a^3\dot{\gamma}/k_B T \simeq 170$ and the particle Reynolds number $Re_p = \rho_p \dot{\gamma} a^2/\eta = 0.125$. The initial configuration of the spherical particle is located at the central position of the system. The volume fraction of a single particle is $\Phi = 0.002$.

An important feature of a single Brownian particle in a simple shear flow is that the MSD in the flow direction varies asymptotically with time as $t^3$. Although we would expect t-dependence of the MSD in the long-time limit, this non-diffusional behavior is explained as a result of a coupling between diffusive motion in the velocity-gradient direction and convective motion due to shear in

the flow direction. Theoretical solutions to this problem show the MSD in the flow direction($x$) is composed of three parts:

$$\langle R_i^x(t)^2\rangle = v_x^2(y_0)t^2 + \langle R_i^x(t)^2\rangle_{\dot\gamma} + \langle R_i^x(t)^2\rangle_0 \tag{5.6}$$

assuming that, at $t = 0$, the particle is in the initial position (0, $y_0$, 0), wherein the first term on the right hand side of Eq. (5.6) is a shear contribution only, and represents the simple translation of a particle along the streamline in the flow direction. The second term is the coupling term described above, which represents the convection induced by diffusion. The third term, which is in the same form as the MSD of a free Brownian particle, is a thermal contribution only. Similar to that of the $x$ direction, the MSDs in the velocity-gradient direction($y$) and the vorticity direction($z$) are derived theoretically; $\langle R_i^y(t)^2\rangle = \langle R_i^y(t)^2\rangle_0$ and $\langle R_i^z(t)^2\rangle = \langle R_i^z(t)^2\rangle_0$. These quantities are determined analytically for a single Brownian particle obeying the normal Langevin equation (LE) or the generalized Langevin equation (GLE) with memory effects.[12–14]

The time evolution of the MSD in the $x$ direction (◯) for a single spherical particle under shear is shown in Fig. 5.2. The MSD was calculated via $\langle|R_i^x(t) - R_i^x(0) - v_x(y_0)t|^2\rangle$ to eliminate the purely shear contribution that corresponds to the first term of Eq. (5.6). The MSD is scaled by $k_BT$. The MSD is in excellent agreement with the analytical solution for the GLE. For short times of up to $t \sim 10^2$, the motion of the Brownian particle in the $x$ direction is like that of a free Brownian particle obeying the GLE. For long times, $t \gg \tau_\nu = 25$, the MSD asymptotically approaches $2D_0\dot\gamma^2t^3/3$, where $D_0 = k_BT/6\pi\eta a$. This $t^3$ regime in the MSD approaches in a much slower manner, $t^{-1/2}$, than that of the analytical solution for the LE. The transient behavior of the MSD depends strongly on whether the memory effects are taken into account.

The MSD $\langle|R_i^z(t) - R_i^z(0)|^2\rangle$ in the $z$ direction (■) is also plotted in Fig. 5.2. The numerical results of the MSD in the $z$ direction agree well with the analytical solution for the GLE of a free Brownian particle where the $t$ regime approaches in a much slower manner, $t^{-1/2}$, and the diffusive motion is attained on time scales of $O(10^4)$. The diffusion time characterizing the diffusive motion is $\tau_D = a^2/D_0 \simeq 3.4 \times 10^4$, which measures the particle diffusion over the particle size.

Another dynamical quantity of interest is the positional cross-correlation $\langle R_i^x(t)R_i^y(t)\rangle$ of a Brownian particle in a simple shear flow. This analytical form is derived for both the LE and GLE. These long-time behaviors show the same dependence on $t$, which is $D_0\dot\gamma t^2$. The cross-correlation was calculated via $\langle(R_i^x(t)-R_i^x(0)-V_i^x(0)t)(R_i^y(t)-R_i^y(0))\rangle$. The numerical results (△) are plotted

in Fig. 5.2 and are in good agreement with the analytical solution for the GLE.

This detailed analysis of the MSD is sufficient to confirm the validity of our method of incorporating memory effects; however, within our method, it is assumed that the thermal fluctuations can be represented by white and gaussian noise. This means that correlations between thermal noise at different times are completely ignored, although in the theoretical framework of the GLE, noises are correlated. The thermal noise memory, which we ignore, is considered to affect the particle's motion on very fast time scales $t < \tau_B \sim 4.5$. On these very short time scales, $t < \tau_B$, a gap between the hydrodynamic analytical solutions and the numerical results is clearly observed in Chapter 3 and 4. Although our method is not applicable to particle motion for $t < \tau_B$, the method can be accurately applied to the motion of particles in a shear flow on time scales $t > \tau_B$, in which the memory effects become significant.

In order to examine the effects of the volume fraction on the short-time motion of Brownian particles in a shear flow, we applied the modified SPM to concentrated dispersions at a finite Reynolds number $Re_p = 0.125$. Concentrated dispersions are of great importance in the rheology of dispersions. Most numerical approaches for such concentrated dispersions are limited to a Reynolds number of zero. Since $Pe \simeq 170$, the hydrodynamic shear forces become dominant over the thermal forces in the particle' motion. The initial configurations of the dispersed particles are randomly distributed. All simulations are performed in an isotropic disorder phase.

Figure 5.3 shows the time evolution of the MSD in the $z$ direction for several volume fractions, up to $\Phi = 0.4$. The time is scaled by $1/\dot{\gamma}$. As the volume fraction is increased, the MSD grows more rapidly in time due to the hydrodynamic and direct interactions between the particles, resulting in a increase in the slope of the MSD for a small strain $\dot{\gamma}t \sim O(10^{-1})$. For $\Phi \geq 0.2$, the diffusive behavior is attained at a smaller strain $\dot{\gamma}t \sim O(1)$ rather than at $\Phi = 0.002$, as for a Brownian particle. The accelerated Stokesian dynamics (ASD) for non-Brownian particles at $\Phi = 0.2$ show the diffusive region is attained at larger strains than at least $10^{15}$ Compared with these numerical results, the onset of the diffusive region in the present simulations is much faster. The time at which the diffusive region is attained shifts to shorter times at higher volume fractions.

The long-time diffusion coefficient $D_z$ was calculated by linearly fitting the data over the diffusion regions. The inset of Fig. 5.3 shows the volume fraction dependence of $D_z$ scaled by $\dot{\gamma}a^2$. The diffusion coefficient increases rapidly up to $\Phi = 0.3$ and reaches a plateau at a volume fraction beyond $\Phi > 0.3$. This behavior of $D_z$ is remarkably different from that at equilibrium, where the

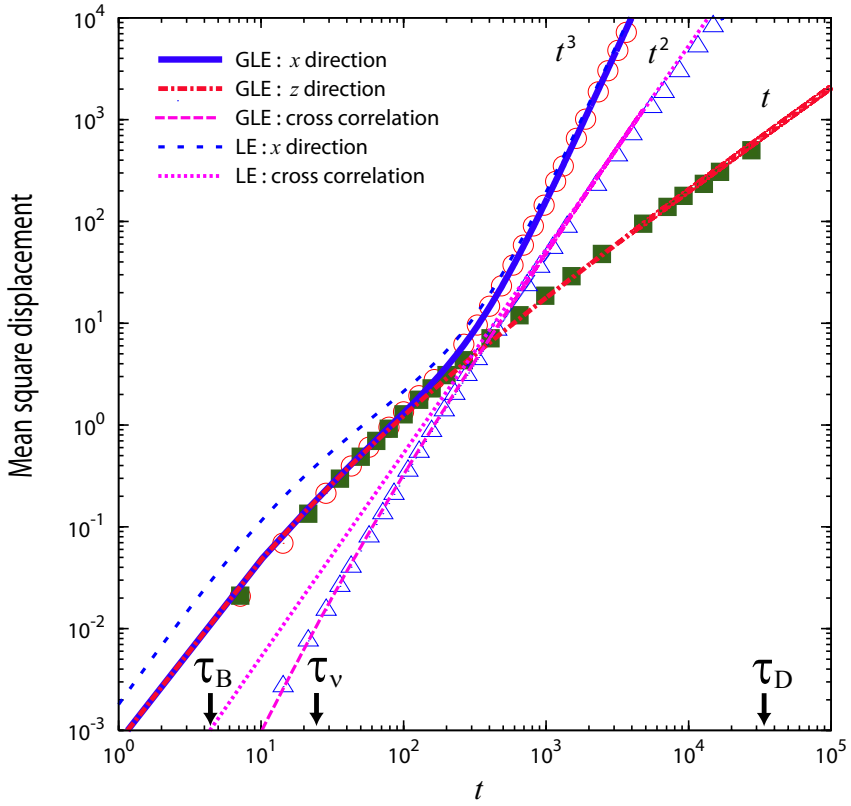


Figure 5.2: Mean square displacement scaled by $k_BT$ of a single spherical particle fluctuating in a Newtonian fluid under shear at $k_BT = 0.07$ and $\dot{\gamma} = 0.005$: (◯) flow direction, (■) vorticity direction, and (△) positional cross-correlation. The analytical solution of the MSD in the flow direction ($x$) for a Brownian particle in a shear flow: the dashed line represents the LE and the solid line the GLE. The dash-dotted line is the analytical solution of the MSD in the vorticity direction ($z$) for the GLE, which is the same form as that for the GLE of a free Brownian particle The analytical solution of the positional cross-correlation for a Brownian particle in a shear flow: the dotted line represents the LE and the dashed line the GLE. The Brownian time $\tau_B \simeq 4.5$, the kinematic time $\tau_\nu = 25$, and the diffusion time $\tau_D \simeq 3.4 \times 10^4$. The parameters for both the particle and fluid are $a = 5$, $\xi = 2$, $\rho_p = 1$, $\rho_f = 1$, and $\eta = 1$. The time unit is $\Delta^2/\nu = 1$, and the length unit is $\Delta = 1$.

diffusion coefficient decreases with increasing volume fraction. The enhancement of the diffusion coefficient with increasing volume fraction is a typical characteristic of shear-induced diffusion coefficients. These results exhibit the same qualitative behavior as the experimental results obtained for non-Brownian particles.[16–18]

## 5.4 Concluding remarks

In conclusion, the short-time motion of Brownian particles in an incompressible Newtonian fluid under shear was examined by using a modified SPM in which external forces are introduced to approximately form a simple shear flow througourt the entire system with periodic boundary con-

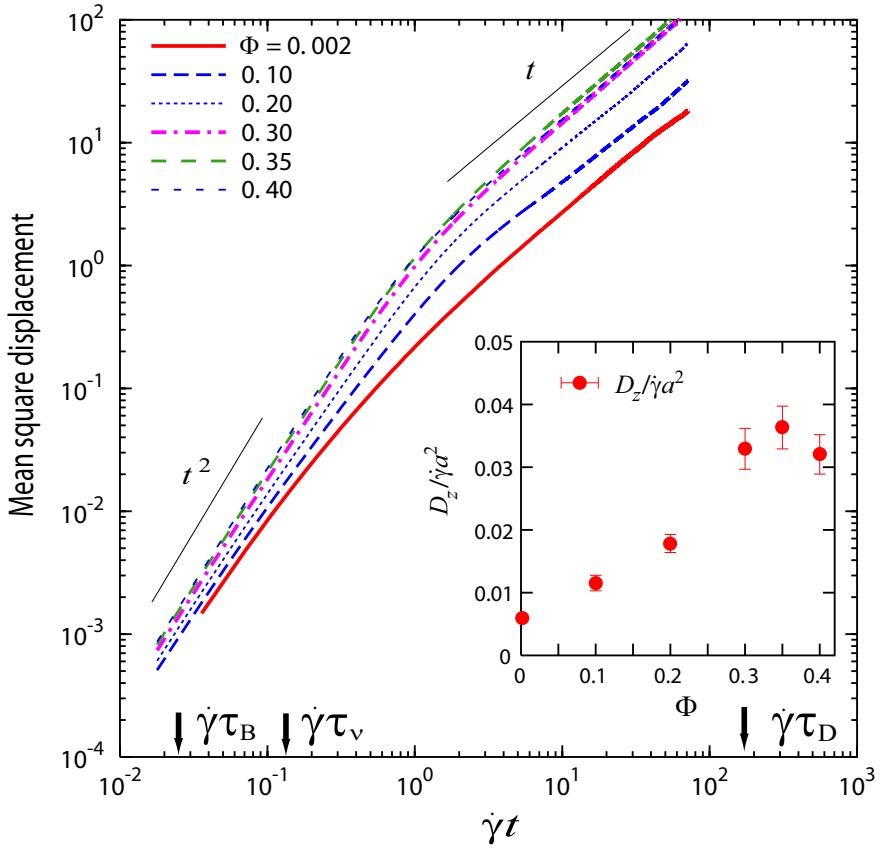


Figure 5.3: The time evolution of the mean square displacement in the vorticity direction ($z$) for several values of the volume fraction $\Phi$ at $k_BT = 0.07$ and $\dot{\gamma} = 0.005$. The Peclet number $Pe \simeq 170$ and the particle Reynolds number $Re_p = 0.125$. The inset shows the volume fraction dependence of $D_z$ scaled by $\dot{\gamma}a^2$. The parameters for both the particle and fluid are $a = 5$, $\xi = 2$, $\rho_p = 1$, $\rho_f = 1$, and $\eta = 1$.

ditions. The validity of the method was carefully examined by comparing the present numerical results for the MSD with the hydrodynamic analytical solution of the GLE of a single Brownian particle in a simple shear flow. In the present study, we aimed to modify the original SPM by incorporating thermal fluctuations so that the modified SPM is valid for $\tau_B < t$, while other computational methods such as Brownian dynamics and ASD, which are based on the LE that ignores memory effects due to fluid motions, are valid only for $\tau_B \ll \tau_D < t$. Simulations were then performed for monodisperse dispersions of repulsive spherical particles at volume fractions ranging from $\Phi = 0.002$-$0.40$. We found that the MSD in the vorticity direction grows rapidly in time and with increasing particle volume fraction. At a strain $\dot{\gamma}t \sim O(1)$, the diffusive region is attained for $\Phi \geq 0.2$. The onset of the diffusive region shifts to shorter times at higher volume fractions. The diffusion coefficient in the vorticity direction was determined from the long-time

behavior of the MSD. For volume fractions of up to 0.3, the diffusion coefficient rises rapidly with increasing volume fraction. It then levels off for volume fractions beyond 0.3. A detailed analysis of the short-time motions in concentrated dispersions is in progress.

# References


1 D. A. Weitz, D. J. Pine, P. N. Pusey, and R. J. A. Tough, Phys. Rev. Lett. **63**, 1747 (1989)

2 J. X. Zhu, D. J. Durian, J. Muller, D. A. Weitz, and D. J. Pine, Phys. Rev. Lett. **68**, 2559 (1992)

3 B. Lukic, S. Jeney, C. Tischer, A. J. Kulik, L. Forro, and E. L. Florin, Phys. Rev. Lett. **95** 160601 (2005).

4 A. J. C. Ladd, Phys. Rev. Lett. **70**, 1339 (1993).

5 H. Tanaka and T. Araki, Phys. Rev. Lett. **85**, 1338 (2000).

6 V. Lobaskin and B. Dünweg, New. J. Phys. **6**, 54 (2004).

7 J. T. Padding and A. A. Louis, Phys. Rev. E. **74**, 031402 (2006).

8 P. J. Atzberger, P. R. Kramer, and C. S. Peskin, J. Comput. Phys. **224**, 1255 (2007).

9 Y. Nakayama, K. Kim, and R. Yamamoto, Eur. Phys. J. E **26**, 361 (2008).

10 Y. Nakayama and R. Yamamoto, Phys. Rev. E **71**, 036707 (2005).

11 N. Sharma and N. A. Patankar, J. Comput. Phys. **201**, (2004) 466.

12 H. J. H. Clercx and P. P. J. M. Schram, Phys. Rev. A. **46**, (1992) 1942.

13 P. P. J. Schram and S. A. Trigger, Physica B **228**, (1996) 91-96.

14 M. Aan Miguel and J. M. Sancho, Physica A **144**, (1979) 357.

15 A. Sierou and J. F. Brady, J. Fluid. Mech. **506** 506 (2004).

16 D. Leighton and A. Acrivos, J. Fluid. Mech. **177**, 109 (1987).

17 V. Breedveld, D. van den Ende, M. Bosscher, R. J. J. Jongschaap, and J. Mellema, Phys. Rev. E **63** 021403 (2001).

18 V. Breedveld, D. Van den Ende, R. J. J. Jongschaap, and J. Mellema, J. Chem. Phys. **114**, 5923 (2001).

# Chapter 6

# Direct numerical simulations for non-Newtonian rheology of concentrated particle dispersions

## 6.1 Introduction

The links between macroscopic rheological properties and microstructures in colloidal dispersions have been extensively investigated for many systems, including dispersions of sterically-stabilized and charged-stabilized particles in host fluids.[1,2]

The behavior of a monodisperse dispersion composed of solid particles immersed in a Newtonian host fluid strongly depends on the volume fraction of the dispersed particles $\Phi$ and the shear rate $\dot{\gamma}$. When the shear rate is zero ($\dot{\gamma} \to 0$), the shear viscosity of the dispersion is referred to as the zero-shear viscosity $\eta_0$. In the dilute limit ($\Phi \ll 1$), the zero shear viscosity is well approximated by Einstein's formula:[3]

$$\eta_0 = \eta(1 + 2.5\Phi), \tag{6.1}$$

where $\eta$ is the shear viscosity of the host fluid. In a concentrated dispersion, theoretical difficulties become rather severe, since the behavior of the dispersed particles is complicated by the interactions between the particles and thermal fluctuations. In particular, the solvent-mediated many-body hydrodynamic interactions (HI) between the particles complicate the dynamical behavior. A number of experiments for concentrated dispersions have been performed to reveal the origin of the non-Newtonian behavior of these dispersions, and several semi-empirical formulas for $\eta_0$ have been proposed to characterize the experimental results. For example, the Krieger-Dougherty relationship:[4]

$$\eta_0 = \eta\Big(1 - \frac{\Phi}{\Phi_m}\Big)^{-[\eta]\Phi_m}, \tag{6.2}$$

where $[\eta]$ is the intrinsic viscosity and $\Phi_m$ is the packing volume fraction at which the viscosity diverges, is often used for fitting the experimental data for uniform colloidal spheres suspended in non-aqueous media.

When a dispersion is subjected to shear ($\dot{\gamma} \neq 0$), the flow properties of the dispersion show a variety of non-Newtonian behaviors, such as shear-thinning and shear-thickening. These non-

Newtonian behaviors are associated with the changing microstructures of the dispersion. Several physical mechanisms for these peculiar behaviors have been proposed; for example, shear-induced order-disorder transitions,[5–7] formations of dynamic clusters of the particles, and other mechanisms. However, a full understanding of the relationships between the rheological properties and the microstructure has not yet been obtained, despite extensive studies.

Computer simulations are very powerful tools in the direct investigation of the dynamics of individual particles in concentrated dispersions. The Stokesian dynamics (SD) method[8] has been widely used to measure the rheology of dispersions and provides valuable information regarding the non-Newtonian behavior of flowing dispersions.[9–12] The SD method, however, is based on the Stokes approximation, which assumes that all relaxation times associated with fluid motions are short as compared with those of the particle, *i.e.*, $\tau_\nu \ll \tau_B$, where $\tau_\nu = \rho_f a^2/\eta$ and $\tau_B = 2\rho_p a^2/9\eta$. Here, $\rho_f$ and $\rho_p$ are the density of the fluid and the particle, respectively, and $a$ is the radius of the particle. With this assumption, the HI is treated as the Ronte-Prager-Yamakawa (RPY) tensor and the lubrication correction. Furthermore, it is assumed that the relaxation time associated with the particle's inertia is ze ro ($\tau_B \to 0$). These approximations are valid for the motion of the particles at time scales much greater than the time scales of the relaxation of both the fluid and the particle inertia. Therefore, the short-time motion of Brownian particles over the kinematic time scale $\tau_\nu$ cannot be described by simulation methods based on the Stokesian approximation.

Sheared dispersions have a non-dimensional parameter that describes the particle's inertia, *e.g.*, the particle Reynolds number $Re_p = \rho_p \dot{\gamma} a^2/\eta = 9\tau_B/2\tau_{\dot{\gamma}}$, where $\tau_{\dot{\gamma}} (= 1/\dot{\gamma})$ represents the characteristic time due to shear. For most colloidal dispersions, the particle Reynolds number is very small. The SD method has a particle Reynolds number of zero and, therefore, cannot be applied to problems with finite particle Reynolds numbers. Typical examples include the motions of dispersions subjected to strong shear or composed of large particles; in these cases, the particle Reynolds number has a relatively large finite value.

Another problem that cannot be treated by the SD method is the short-time motion of the particle, in which the fluid inertia becomes significant even if the particle Reynolds number is very small. For example, the characteristic time scale is $\tau_\nu \sim 1$ $\mu$s for a neutrally buoyant particle of 1 $\mu$m in water, and $Re_p \sim 10^{-8}$ for $\dot{\gamma} = 0.01$. The effects of the fluid inertia appear as memory effects of the particles. For a complete understanding of these flowing dispersions, full time-dependent HIs are required.

In recent years, several numerical methods have been developed in order to accurately simulate dispersions in a variety of situations, including those described above. These methods of dispersion modeling are based on the same approach, which involves resolving the fluid motion simultaneously with the particle motion. We refer to this approach as the direct numerical simulation (DNS) approach. This approach enables us to accurately treat the full time-dependent HI. The numerical methods differ mainly in the approach used to solve the motion of the host fluid - the lattice Boltzmann method,[13] stochastic rotation dynamics,[14] and the finite element method,[15] for example.

In this work, we apply a direct numerical scheme based on the smoothed profile method (SPM)[?,16,17] to a monodisperse concentrated dispersion of repulsive and neutrally buoyant Brownian particles in a shear flow. In the SPM, the Navier-Stokes equation for the fluid motion is discretized on a regular grid, and the Newtonian equations for the particle motion are solved simultaneously with the Navier-Stokes equations for the fluid motion. For distances less than the lattice spacing, the lubrication force is not included, due to the space resolution in this work. This developed scheme accounts for thermal fluctuations, a shear flow, and memory effects. The SPM can reproduce the correct short-time behavior of a single Brownian particle in a shear flow on the kinematic time scale, and the numerical tests were reported in Chapter 5.

Although some groups have studied flowing dispersions by using a DNS method based on LBM,[18–20] all the simulations have been applied to a dispersion of non-Brownian particles and ignore the thermal fluctuations of the particles. In these studies, shear-thickening behavior was demonstrated for the apparent shear viscosity for $Re_p > 1$. However, a direct analysis of the simulation results for the shear-thickening has not been fully performed.

In the present study, our main goal is to clarify the origin of the non-Newtonian behavior of the concentrated dispersion by using a DNS method, accounting for thermal fluctuations and a shear flow. Note that the simulated situations are different from those of the prevailing experiments for colloidal dispersions, since even the lowest particle Reynolds number in these simulations is several hundred times larger than those of the experiments. We first present the simulation method and the manner in which the apparent shear viscosity of the dispersions is calculated. Three-dimensional simulations are performed with periodic boundary conditions, and the non-Newtonian behavior of the shear viscosity is obtained for several volume fractions. Both the high and low shear limiting viscosities obtained from the simulations are then compared with the Krieger-Doughty relationship. Next, we concentrate on the shear-thickening for $Re_p > 1$, so as to quantitatively describe the

thickening behavior. Several contributions to the apparent shear viscosity are examined. Finally, the long-time diffusion coefficients are measured from the long-time behavior of the mean square displacement.

## 6.2 Simulation Method

A direct numerical scheme that implements both a shear flow and thermal fluctuations is briefly explained. A more detailed explanation is given in Chapter 5. We consider a monodisperse dispersion of $N_p$ repulsive spherical particles of diameter $\sigma$ in a Newtonian host fluid. The particles interact via a truncated Lennard-Jones potential:

$$U_{LJ}(r) = \begin{cases} 4\epsilon\left[\left(\frac{\sigma}{r}\right)^{36} - \left(\frac{\sigma}{r}\right)^{18}\right) + \frac{1}{4}\right] & (r < 2^{1/18}\sigma), \\ 0 & (r > 2^{1/18}\sigma), \end{cases} \tag{6.3}$$

where $r$ is the distance between two particles and the parameter $\epsilon$ characterizes the interaction strength. The position of the $i$th dispersed particle is $\boldsymbol{R}_i$, the translational velocity is $\boldsymbol{V}_i$, and the rotational velocity is $\boldsymbol{\Omega}_i$. The time evolution of the $i$th particle with mass $M_i$ and moment of inertia $\boldsymbol{I}_i$ is governed by Newton's equations of motion:

$$M_i \dot{\boldsymbol{V}}_i = \boldsymbol{F}_i^H + \boldsymbol{F}_i^C + \boldsymbol{G}_i^V, \quad \dot{\boldsymbol{R}}_i = \boldsymbol{V}_i, \tag{6.4}$$

$$\boldsymbol{I}_i \cdot \dot{\boldsymbol{\Omega}}_i = \boldsymbol{N}_i^H + \boldsymbol{G}_i^\Omega, \tag{6.5}$$

where $\boldsymbol{F}_i^H$ and $\boldsymbol{N}_i^H$ are the hydrodynamic forces and torques exerted by the host fluid on the particle. $\boldsymbol{F}_i^C$ is a repulsive force arising from the potential of Eq.(6.3), which prevents the particles from overlapping. $\boldsymbol{G}_i^V$ and $\boldsymbol{G}_i^\Omega$ are random forces and torques, respectively, due to thermal fluctuations. These random fluctuations are assumed to be Markovian (white or time delta-correlated) and determine the particle temperature $T$. The procedure for determining the temperature is described in Chapter .

In the SP method, the velocity and pressure fields, $\boldsymbol{v}(\boldsymbol{x}, t)$ and $p(\boldsymbol{x}, t)$, are defined on three-dimensional Cartesian grids, which consist of fluid and particle domains. In order to distinguish the particle and fluid domains on the grids, a smoothed function $\phi(\boldsymbol{x}, t)$, which is equal to 1 in the particle domains and 0 in the fluid domains, is introduced. These domains are separated by a thin interfacial domain of thickness $\xi$. The system size is $[0, L_x] \times [-L_y/2, L_y/2] \times [0, L_z]$.

The time evolution of the velocity field is governed by the Navier-Stokes equation with the

incompressibility condition $\nabla \cdot \boldsymbol{v} = 0$:

$$\rho_f(\partial_t \boldsymbol{v} + \boldsymbol{v} \cdot \nabla \boldsymbol{v}) = \nabla \cdot \boldsymbol{\sigma} + \rho_f \phi \boldsymbol{f}_p + \rho_f \boldsymbol{f}^{shear}, \tag{6.6}$$

where the stress tensor $\boldsymbol{\sigma} = -p\boldsymbol{I} + \eta\{\nabla \boldsymbol{v} + (\nabla \boldsymbol{v})^T\}$, and $\boldsymbol{f}^{shear}(\boldsymbol{x}, t)$ is an external force field that is introduced to enforce a simple shear flow on the system. The external force is introduced as a constraint force so that the velocity field satisfies $v_x(y) = -\dot{\gamma} L_y/4$ at $y = -L_y/4$ and $v_x(y) = \dot{\gamma} L_y/4$ at $y = L_y/4$, where $y$ denotes the distance in the velocity gradient direction. A simple shear flow with a shear rate of $\dot{\gamma}$ is then approximately produced over a range from $y = -L_y/4$ to $y = L_y/4$. $\phi \boldsymbol{f}_p$ represents a body force that ensures the rigidity of the particles and the appropriate non-slip boundary conditions at the fluid/particle interface, which is further elaborated upon in reference.[16,17]

The length unit is taken to be the lattice spacing $\Delta$ and the time unit is $\tau_0 = \rho_f \Delta^2/\eta$. The second-order Runge-Kutta algorithm is used to integrate the Newtonian equations. The Navier-Stokes equation is discretized with a Fourier spectral scheme in space and with a second-order Runge-Kutta scheme in time. The discretized time step is $h = 0.07145\tau_0$, and this value is set to be very small as compared to $\tau_M = (M_i \sigma^2/\epsilon)^{1/2}$. $\tau_M$ is often used as a time unit in normal molecular-dynamics simulations. For the numerical parameters used in this work, $\tau_0 = 1$ and $\tau_M \sim 131$: $\Delta = 1$, $\eta = 1$, $\rho_f = 1$, $\rho_p = 1$, $\epsilon = 1$, $a = 4$, and $\sigma = 8$.

To measure the rheology of dispersions in a shear flow, we can calculate the apparent stress $\boldsymbol{\sigma}^{eff}$ of the dispersions in the following manner. The equation of the momentum of a dispersion in a shear flow is formally written as:

$$\frac{d}{dt}(\rho_t \boldsymbol{v}) = \nabla \cdot \boldsymbol{\sigma}^{dis} + \rho_t \boldsymbol{f}^{shear}, \tag{6.7}$$

$$\rho_t = (1 - \phi)\rho_f + \phi \rho_p, \tag{6.8}$$

where $\boldsymbol{\sigma}^{dis}$ denotes the local stress of the dispersion. Although $\boldsymbol{\sigma}^{dis}$ cannot be calculated directly,

we can obtain the apparent stress $\boldsymbol{\sigma}^{eff}$ by using the local stress $\boldsymbol{\sigma}^{dis}$:

$$\boldsymbol{\sigma}^{eff} = \frac{1}{V}\int d\boldsymbol{x}\boldsymbol{\sigma}^{dis} \tag{6.9}$$

$$= \frac{1}{V}\int d\boldsymbol{x}\Big[[\nabla\cdot(\boldsymbol{\sigma}^{dis}\boldsymbol{x})]^T - \boldsymbol{x}\nabla\cdot\boldsymbol{\sigma}^{dis}\Big] \tag{6.10}$$

$$= \frac{1}{V}\int d\boldsymbol{x}[-\boldsymbol{x}\nabla\cdot\boldsymbol{\sigma}^{dis}] \tag{6.11}$$

$$= \frac{1}{V}\int d\boldsymbol{x}\Big[\boldsymbol{x}\Big(\rho_t\boldsymbol{f}^{shear} - \frac{d}{dt}(\rho_t\boldsymbol{v})\Big)\Big] \tag{6.12}$$

$$= \frac{1}{V}\int d\boldsymbol{x}\boldsymbol{x}\rho_t\boldsymbol{f}^{shear} - \frac{1}{V}\int d\boldsymbol{x}\boldsymbol{x}\frac{d}{dt}(\rho_t\boldsymbol{v}), \tag{6.13}$$

with a volume $V = L_xL_yL_z$. In the derivation of Eq.(6.10), we use an second rank identity, $\boldsymbol{\sigma}^{dis} = [\nabla\cdot(\boldsymbol{\sigma}^{dis}\boldsymbol{x})]^T - \boldsymbol{x}\nabla\cdot\boldsymbol{\sigma}^{dis}$. In the steady state,

$$\Big\langle\frac{d}{dt}(\rho_t\boldsymbol{v})\Big\rangle_t = 0, \tag{6.14}$$

where $\langle\rangle_t$ denotes time averaging over the steady state. The time-averaged apparent shear stress of the dispersion can then be written as:

$$\langle\boldsymbol{\sigma}^{eff}\rangle_t = \frac{1}{V}\Big\langle\int d\boldsymbol{x}\boldsymbol{x}\rho_t\boldsymbol{f}^{shear}\Big\rangle_t. \tag{6.15}$$

## 6.3 simulation Results

Simulations were performed in a three-dimensional cubic box with periodic boundary conditions. The length of the system is $L_x = L_y = L_x = 64$. For a spherical particle, $a = 4$, $\xi = 2$. The temperature was determined by equilibrium calculations before the shear flow was imposed. The temperature is $k_BT = 7$. The initial configuration of the particles is set to be a random distribution. A large number of simulations were performed for volume fractions of $0.31 \leq \Phi \leq 0.56$ and shear rates of $5\times10^{-5} \leq \dot{\gamma} \leq 0.5$. These systems have particle Reynolds numbers $Re_p$ ranging from $8\times10^{-4}$ to 16.

### 6.3.A The rheology of a concentrated dispersion in a shear flow

For dispersions composed of Brownian particles in the steady state, the apparent shear viscosity of the dispersion is defined as:

$$\eta^{eff} = \frac{\langle\sigma_{xy}^{eff}\rangle_t}{\dot{\gamma}}, \tag{6.16}$$

where $\sigma_{xy}^{eff}$ denotes the $xy$-components of $\boldsymbol{\sigma}^{eff}$.

Figure 6.1 shows the dependence of the apparent shear viscosity on the Peclet number for several volume fractions. Here, the Peclet number is defined as $Pe = 6\pi\eta a^3\dot{\gamma}/k_BT$. For the lowest concentration ($\Phi = 0.31$), the viscosities remain nearly constant and exhibit Newtonian behavior. For higher concentrations ($\Phi \geq 0.41$), the dispersions show non-Newtonian behaviors such as strong shear-thinning at low Peclet numbers and shear-thickening at high Peclet numbers. As $Pe$ increases, the shear-thinning behavior is clearly observed from the higher plateau region for $Pe$ of order $10^{-2}$ to a lower plateau region for $Pe$ of about 10. From both of the plateau values of the viscosity curve, we can obtain the low shear limiting viscosity (identified as $\eta_0$) and the high shear limiting viscosity $\eta_\infty$ for each volume fraction.

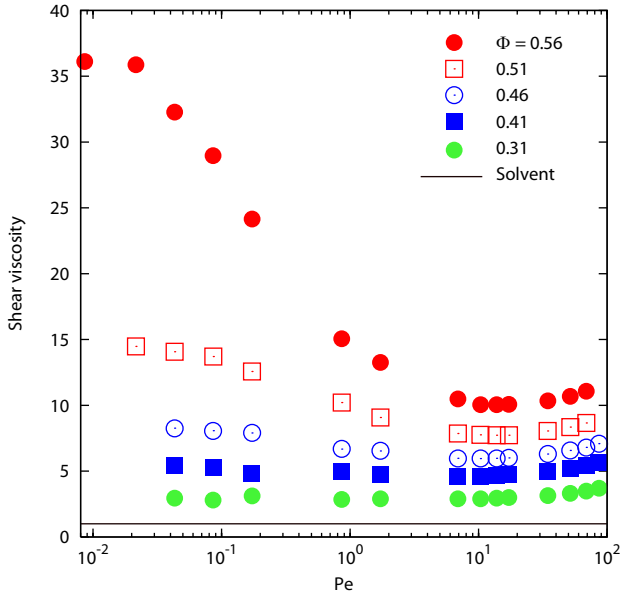


Figure 6.1: Peclet number dependence of the apparent shear viscosity of the dispersion for several volume fractions. The solid line represents the shear viscosity of the host fluid.

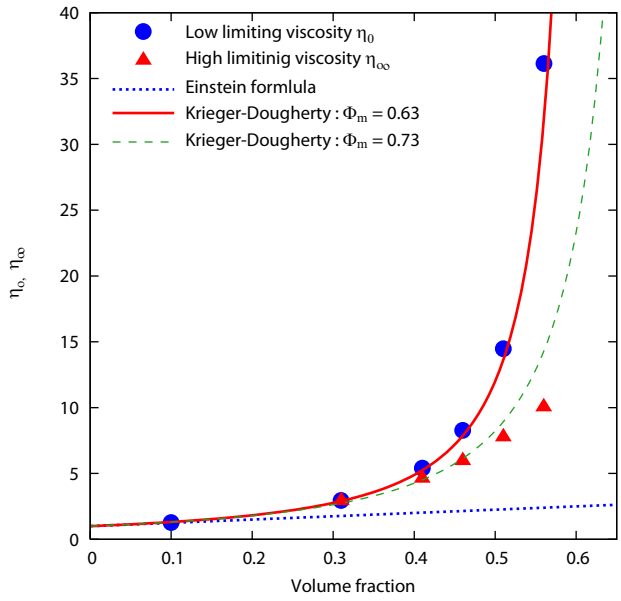


Figure 6.2: Volume fraction dependence of the low shear limiting viscosity $\eta_0$ and the high shear limiting viscosity $\eta_\infty$ of the dispersions. The solid line represents the Krieger-Dougherty relationship with $\Phi_m = 0.63$ for $\eta_0$ and the dashed line $\Phi_m = 0.73$ for $\eta_\infty$. The dotted line represents Einstein ' s formula of Eq.(6.1).

Figure 6.2 shows the dependence of the low shear limiting viscosity $\eta_0$ and the high shear limiting viscosity $\eta_\infty$ on the volume fraction. Both shear limiting viscosities increase monotonically with the volume fraction. The simulation results for both of the shear limiting viscosities agree well with the semi-empirical relations of Eq.(6.2) by Krieger-Dougherty, $\eta_{0,\infty} = \eta(1-\Phi/\Phi_m)^{-2.5\Phi_m}$ where $\Phi_m = 0.63$ for $\eta_0$ and $\Phi_m = 0.73$ for $\eta_\infty$. The dotted line represents Einstein 's formula of Eq.(6.1).

Next, we focus on the viscosity curve in Fig. 6.1 for the high Peclet number region, for which the hydrodynamic shear forces become dominant over the thermal forces in the particle's motion. Figure 6.3 displays a magnification of Fig. 6.1. In Fig. 6.3(a), all of the viscosities show a shear-thickening behavior for $Pe \gtrsim 17$. The onset of the shear-thickening corresponds to $Re_p \sim 1.6$. When $\Phi = 0.31$, the viscosity is almost constant at low Peclet numbers but increases after reaching a Peclet number of about 10. When $\Phi \geq 0.41$, the viscosities decrease at low Peclet numbers but increase after reaching a Peclet number of about 10. This thickening behavior for $Re_p > 1$ is in agreement with the two-dimensional simulation results of Shakib-Manesh *et al.*[18] and Kromkamp *et al.*[19] and the three-dimensional simulation of Kulkami and Morris.[20]

In order to describe the thickening behavior for all volume fractions, we use the following

function of the shear rate and the volume fraction:

$$\eta_f(\dot{\gamma}, \Phi) \cong \eta_\infty(\Phi) + g(\Phi)\dot{\gamma}, \tag{6.17}$$

where $g(\Phi)$ is a function of the volume fraction and $\eta_\infty(\Phi)$ is the high shear limiting viscosity obtained from the simulation. The function $\eta_f$ for each volume fraction (solid lines) is plotted as a function of the Peclet number in Fig. 6.3(a). These solid lines fit well with the simulation data in the thickening regions. Figure 6.3(b) represents the log-log plot of $\Delta\eta = \eta^{eff} - \eta_\infty$ versus $\dot{\gamma}$ for $\dot{\gamma} > 0.01$ ($Re_p \geq 1.6$). We found that $\Delta\eta$ increases linearly at high shear rates for all volume fractions. The solid lines in Fig. 6.3(b) represent $g(\Phi)\dot{\gamma}$ for each volume fraction. The inset of Fig.6.3(b) shows the volume fraction dependence of $g(\Phi)$. We found that $g(\Phi)$ increases monotonically with increasing volume fraction. These results indicate that the apparent shear stress of the dispersion is proportional to the square of the strain rate, $\sigma^{eff} \propto \dot{\gamma}^2$, at high shear rates. This behavior is similar to the Bagnold scaling of dense granular materials.

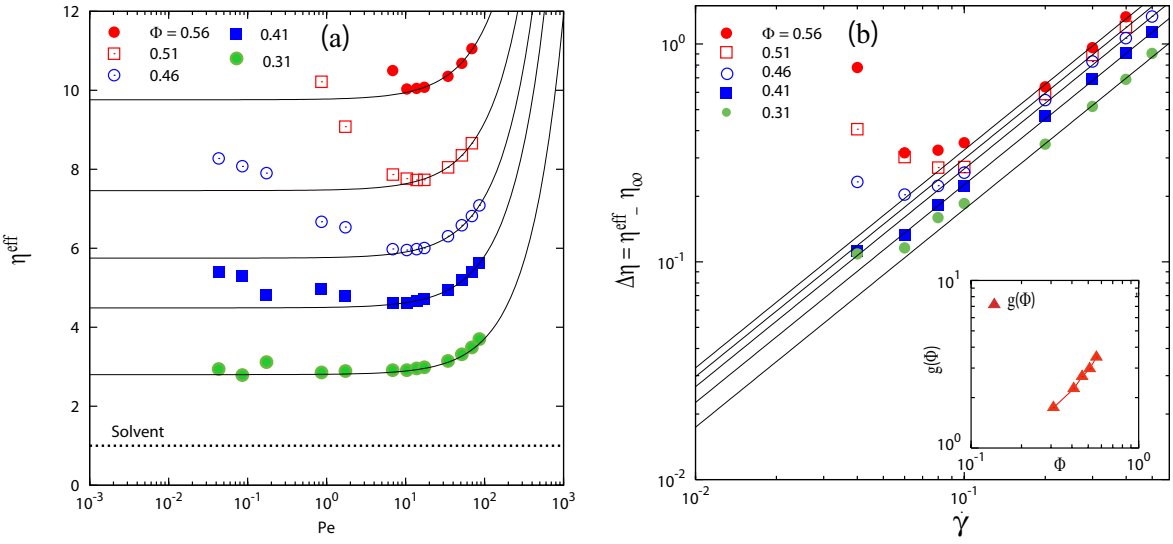


Figure 6.3: (a) Peclet number dependence of the apparent shear viscosity $\eta_{eff}$ for several volume fractions. The solid lines represent $\eta_f$=$\eta_\infty(\Phi) + g(\Phi)\dot{\gamma}$ for each volume fraction. (b) Shear rate dependence of $\Delta\eta = \eta^{eff} - \eta_\infty$ for $\dot{\gamma} > 0.01$ ($Pe > 17.2$). The solid lines represent the lines of $g(\Phi)\dot{\gamma}$ for each volume fraction. The inset shows the volume fraction of $g(\Phi)$.

The apparent shear stress is composed of several microscopic components. Several contributions to the apparent shear stress can be directly calculated. The direct interparticle contribution is defined as

$$\sigma_{xy}^{direct} = \frac{1}{2V} \sum_{i \neq j} \frac{r_{ij}^x r_{ij}^y}{r_{ij}} U'_{LJ}(r_{ij}), \tag{6.18}$$

where $r_{ij}^x$ and $r_{ij}^y$ are the $x$ and $y$ components of the vector $\boldsymbol{r}_{ij}$ between the $i$th and $j$th particle. This stress represents the stress caused by elastic particle-particle collisions. The fluid and particle inertia contribution can be written as

$$\sigma_{xy}^{inertia} = \frac{1}{V} \int d\boldsymbol{x} \rho_t v_x v_y, \tag{6.19}$$

which is similar to the Reynolds stress of a uniform fluid in turbulence. This stress represents the strength of the hydrodynamic instability. Using the shear stresses defined above, we can decompose the apparent shear viscosity into four parts.

$$\eta^{eff} = \eta + \eta^{direct} + \eta^{inertia} + \eta^{hydro}, \tag{6.20}$$

where $\eta^{direct}$ denotes the direct interparticle contribution to the apparent shear viscosity, $\eta^{inertia}$ denotes the inertia contribution, and $\eta^{hydro}$ denotes the hydrodynamic contribution that includes the HI and the lubrication force. The hydrodynamic contribution can be indirectly calculated via $\eta^{hydro} = \eta^{eff} - (\eta + \eta^{direct} + \eta^{inertia})$.

Figure 6.4 shows the individual contributions to the apparent shear viscosity for $\Phi = 0.31, 0.41, 0.46,$ and 0.51. We found that the shear-thinning of the apparent shear viscosity is caused mainly by the decrease in the direct interparticle component. When $\Phi = 0.51$, the direct interparticle component is greater than the hydrodynamic component at low Peclet numbers but is smaller at Peclet numbers greater than 10. When $\Phi = 0.46$, both the direct and hydrodynamic contributions are comparable at low Peclet numbers, but the hydrodynamic component becomes greater than the direct interparticle component at Peclet numbers greater than $10^{-1}$. When $\Phi \leq 0.41$, the hydrodynamic component is greater than the direct interparticle component over the entire range of Peclet numbers. For the thickening regions, all the components gradually increase, resulting in a linear increase in the apparent shear viscosity. Interestingly, the inertia component shows almos t the same behavior, independent of the volume fraction, although the values are very small. The values of the inertia component are shown in Table 1. This thickening behavior may suggest an enhanced increase in the viscosity, due to the hydrodynamic instability for $Re_p > 1$.

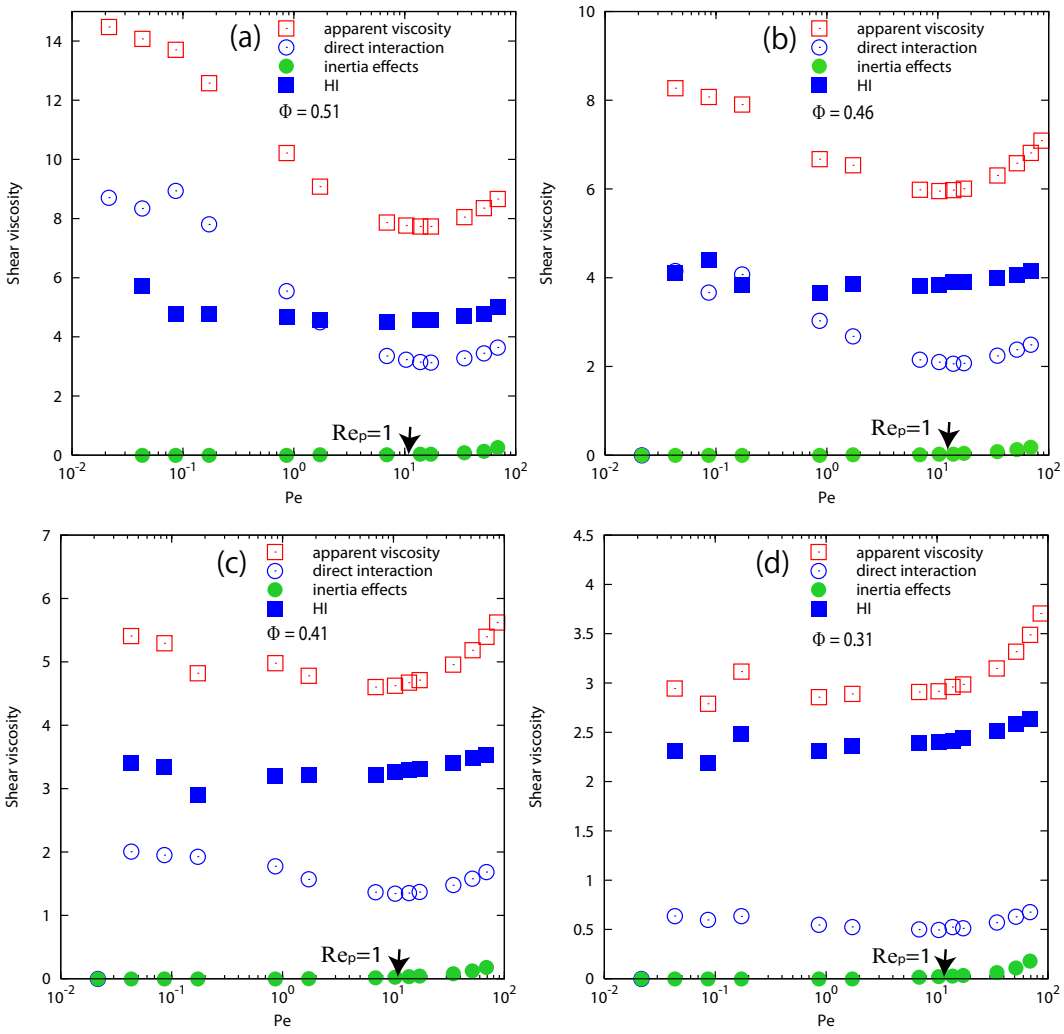


Figure 6.4: Several contributions to the apparent shear viscosity for the volume fraction (a) 0.51, (b) 0.46, (c) 0.41, and (d) 0.31: (□) apparent shear viscosity, (■) hydrodynamic component, (○) direct interparticle component, (•) inertia component.

### 6.3.B The dynamics of the Brownian particles in a shear flow

Finally, we examine the dynamical motion of Brownian particles in a shear flow. We analyze the mean square displacement (MSD) in the vorticity direction ($z$) for the Brownian particles,

$$\langle [\Delta R_z(t)]^2 \rangle = \frac{1}{N_p} \sum_{j=1}^{N_p} \langle |R_j^z(t) - R_j^z(0)|^2 \rangle. \tag{6.21}$$

Figure 6.5 shows the MSD of the dispersion with the lowest Peclet number for each volume fraction. These results are considered to be the MSD at thermal equilibrium. As the volume fraction is increased, the dynamical behavior of the MSD varies greatly, as compared with that of the analytical solution for a single Brownian particle in a shear flow. For $\Phi = 0.56$, we found that a clear plateau

| $\dot{\gamma}$ ($Re_p$) | $\Phi = 0.31$ | $\Phi = 0.41$ | $\Phi = 0.51$ |
|---|---|---|---|
| 0.04 (0.64) | $1.69\times10^{-2}$ | $1.47\times10^{-2}$ | $1.12\times10^{-2}$ |
| 0.08 (1.28) | $2.82\times10^{-2}$ | $3.11\times10^{-2}$ | $2.87\times10^{-2}$ |
| 0.10 (1.6) | $3.29\times10^{-2}$ | $3.99\times10^{-2}$ | $3.59\times10^{-2}$ |
| 0.20 (3.2) | $6.32\times10^{-2}$ | $7.82\times10^{-2}$ | $8.06\times10^{-2}$ |
| 0.30 (4.8) | $1.08\times10^{-1}$ | $1.24\times10^{-1}$ | $1.26\times10^{-1}$ |
| 0.40 (6.4) | $1.80\times10^{-1}$ | $1.77\times10^{-1}$ | $1.76\times10^{-1}$ |

Table 6.1: A list of the inertia viscosity $\sigma^{inertia}$ values for different shear rates and volume fractions. The values have errors of less than a few percent.

region exists for the time scale of order $10^2$. The time at which the plateau region is attained is slightly greater than the kinematic time $\tau_\nu$. This behavior at the highest $\Phi$ indicates the existence of glassy states, *e.g.*, colloidal glass.

The Peclet number dependence of the MSD is plotted in Fig. 6.6 for (a) $\Phi = 0.31$ and (b) $\Phi = 0.56$. As the Peclet number is increased, the MSD for both volume fractions grows more rapidly, and the diffusive behavior is attained at shorter times. We found that the dynamical motion of Brownian particles for $\Phi = 0.56$ is greatly enhanced by shear flows, as compared with that for $\Phi = 0.31$.

The long-time diffusion coefficient $D_z$ in the vorticity direction can be calculated via

$$D_z = \lim_{t\to\infty} \frac{1}{2t}\langle[\Delta R_z(t)]^2\rangle. \tag{6.22}$$

Figure 6.7 shows the Peclet number dependence of $D_z(\Phi)$, normalized by $D_0 = k_BT/6\pi\eta a$, for several volume fractions. For the low Peclet number region, the diffusion coefficient decreases with increasing volume fraction, and this dependence is similar to that of the dispersion at thermal equilibrium. On the other hand, for Peclet numbers greater than 10, the diffusion coefficient increases with the volume fraction. This behavior indicates shear-induced diffusion. The dynamics of the Brownian particles differs considerably, depending on whether the thermal or shear force is dominant. The volume fraction dependence is in qualitative agreement with the numerical results achieved based on the SD method, which is valid for long time scales.[9] As the Peclet number increases, the diffusion coefficient for $\Phi \geq 0.41$ clearly increases. When $\Phi = 0.31$, the diffusion coefficient remains nearly constant, but above $Pe > 10$, it increases linearly. W e note that the diffusion coefficient for each volume fraction increases linearly above $Re_p > 1$.

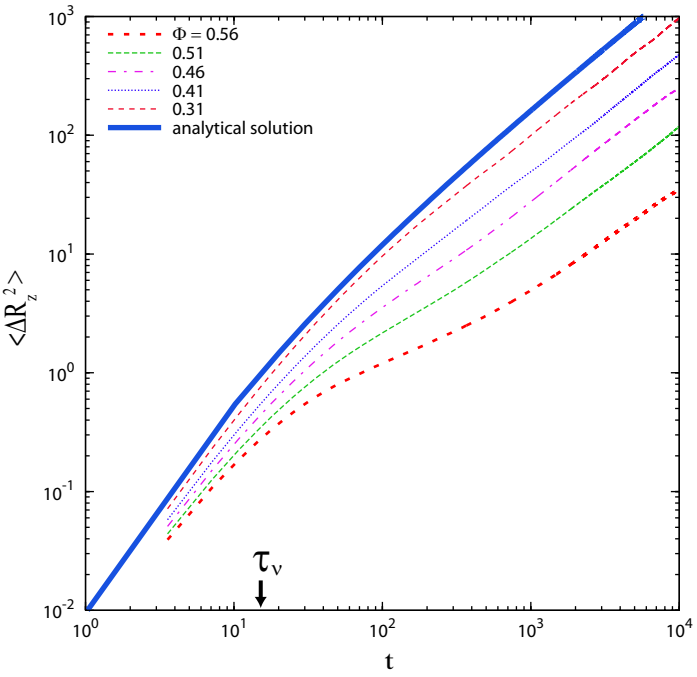


Figure 6.5: The mean square displacement at values of $Pe$ less than $10^{-1}$ for each volume fraction. For $\Phi = 0.56, 0.51$, the data for a $Pe$ of 0.043 was used, and for $\Phi \leq 0.46$, the data for a $Pe$ of 0.086 was used. The solid line represents the analytical solution for the generalized Langevin equation of a free Brownian particle. The arrow indicates the kinematic time $\tau_\nu = \eta a^2/\rho_f = 16$.

## 6.4 Conclusions

We investigated the rheological properties of monodisperse concentrated dispersions with repulsive spherical particles by using a DNS method that accounted for a shear flow and thermal fluctuations. We observed that the apparent shear viscosity shows non-Newtonian behaviors such as shear-thinning at low Peclet numbers and shear-thickening at high Peclet numbers. The apparent viscosity for $\Phi = 0.31$ is almost constant when $Pe < 10$ but increases linearly when $Pe > 10$. For $\Phi \geq 0.41$, the viscosities decrease at low Peclet numbers but increase linearly when $Pe > 10$. From the viscosity versus Peclet number curves, we can obtain both the low and high limiting viscosities, and these results are in good agreement with the Krieger-Doughty relationship. The shear-thickening behavior occurs at particle Reynolds numbers $Re_p > 1$ for all volume fractions. In the thickening regions, the viscosity is proportional to the shear rate, and its slope increases monotonically with increasi ng volume fraction. The shear-thinning of the apparent shear viscosity is caused mainly by the decrease in the direct interparticle contribution. The inertia contributions throughout the entire range of Peclet numbers is very small, as compared with the other contributions. As the volume fraction increases, the behavior of the MSD in the vorticity direction deviates from the

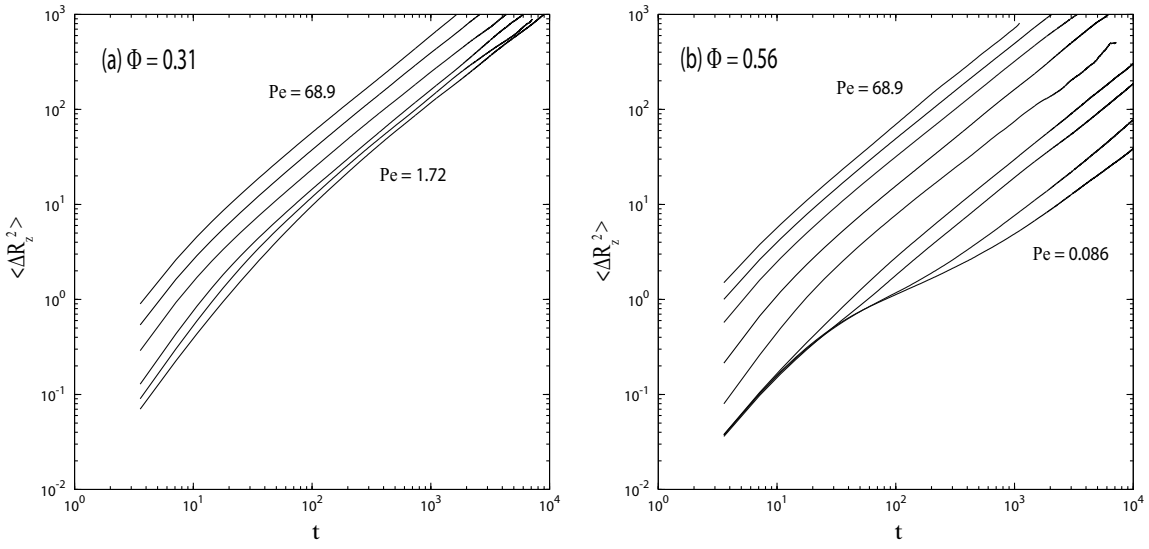


Figure 6.6: The Peclet number dependence of the mean square displacement in the vorticity direction. (a) $\Phi = 0.31$. The Peclet number $Pe$ is 1.72, 10.3, 17.2, 34.4, 51.6, and 68.9 from the bottom. (b) $\Phi = 0.56$. The Peclet number $Pe$ is 0.086, 0.17, 0.86, 1.72, 6.89, 17.2, 34.4, 51.6, and 68.9 from the bottom.

analytical solution for a single Brownian particle in a shear flow. For $\Phi = 0.56$, a glassy state was observed. The diffusion coefficient for high volume fractions increases more than that of low volume fractions with increasing Peclet number. For all volume fractions, the diffusion coefficient begins to increase linearly at $Re_p \sim 1$.

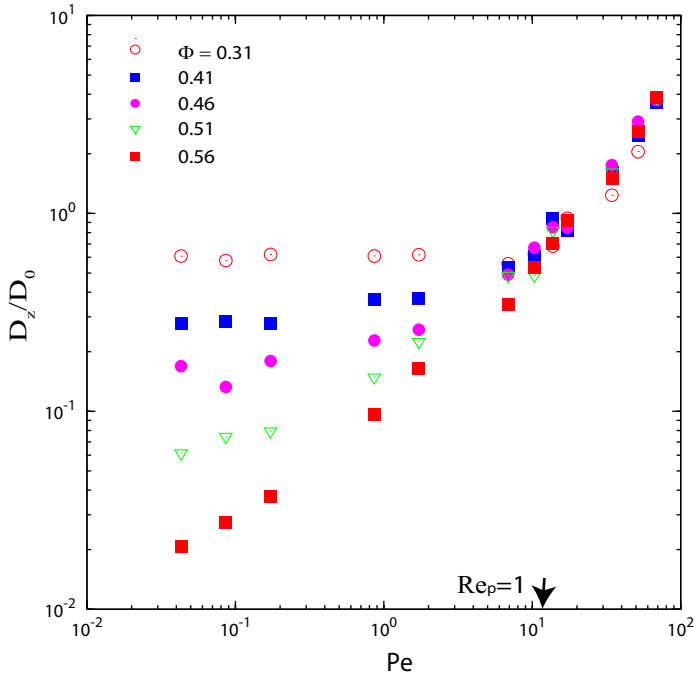


Figure 6.7: The long-time diffusion coefficient in the vorticity direction for different Peclet numbers and volume fractions. The diffusion coefficient is scaled by $D_0 = k_B T/6\pi\eta a$.

## References


1 W. B. Russel, D. A. Saville, W. R. Schowalter, *Colloidal dispersions* (Cambridge University Press, Cambridge, UK, 1989).

2 R. G. Larson, *The Structure and Rheology of Complex Fluids* (Oxford University Press, Oxford, 1999).

3 A. Einstein, Ann. Phys. (Leipzig) **17**, 459 (1905)

4 I. M. Krieger and T. J. Doughty, Trans. Soc. Rheol. **3**, 137 (1957).

5 R. L. Hoffman, Trans. Soc. Rheol. **16**, 155 (1972)

6 B. J. Ackerson and P. N. Pusey, Phys. Rev. Lett. **61**, 1033 (1988)

7 M. D. Haw, W. C. Poon, Phys. Rev. E **57**, 6859 (1998)

8 J. F. Brady, G. Bossis, Ann. Rev. Fluid Mech. **20**, 111 (1988).

9 D. R. Foss and J. F. Brady, J. Fluid Mech. **407**, 167 (2000)

10 A. Sierou and J. F. Brady, J. Fluid Mech. **506**, 285 (2004)

11 D.I. Dratler and W. R. Schowalter, J. Fluid Mech. **325** 1 (1996)

12 D.I. Dratler, W. R. Schowalter, and R. L. Hoffman, J. Fluid Mech. **353** 1 (1997)

13 A. J. C. Ladd, Phys. Rev. Lett. **70**, 1339 (1993).

14 J. T. Padding and A. A. Louis, Phys. Rev. E **74**, 031402 (2006).

15 Masahiro Fujita and Yukio Yamaguchi, Phys. Rev. E **77** 026706 (2008).

16 Y. Nakayama and R. Yamamoto, Phys. Rev. E **71**, 036707 (2005).

17 Y. Nakayama, K. Kim, and R. Yamamoto, Eur. Phys. J. E **26**, 361 (2008).

18 A. Shakib-Manesh, P.Raiskinmaki, A. Koponen, and M.Kataja, and J.Timonen, J. Stat. Phys. **107**, 67 (2002).

19 J. Kromkamp, D. T. M. van den Ende, D. Kandhai. R. G. M. van der Sman, and R. M. Boom, J. Fluid Mech. **529**, 253 (2005)

20 P. M. Kulkarmi and J. F. Morris, Phys. Fluids **20**, 040602 (2008)

# Chapter 7

# General conclusion

In order to investigate the dynamical behaviors of granular pastes and colloidal dispersions, several numerical models are proposed. This dissertation is composed of seven chapters as follows:

In **Chapter 2**, we proposed the dynamics of a sweeping interface and constructed a model based on the phase field. Numerical simulations were performed, demonstrating that the flat interface becomes unstable and that a pattern was produced after the interface passes.

In **Chapter 3** , we developed a numerical method for consistently implementing thermal fluctuations and hydrodynamic interactions into models of the motions of Brownian particles dispersed in incompressible host fluids. We represented the thermal fluctuations by random forces acting on the Brownian particles and the hydrodynamic interactions by directly resolving the fluid motions. The validity of the method has been carefully examined by comparing the present numerical results with the fluctuation−dissipation theorem for a dispersion of a single spherical particle. Simulations were then performed for dispersions of many spherical particles as well as for a polymeric chain in a fluid. In the former case, we found that the hydrodynamic long-time tail in the VACF−clearly observed for a single particle dispersion− becomes weak with increasing volume fraction of the particles. In the latter case, we found that our numerical results coincide quite well with the theoretical predictions of the Zimm model.

In **Chapter 4**, we proposed a numerical model to simulate Brownian particles fluctuating in Newtonian host fluids. To test the validity of the model, the translational velocity autocorrelation function (VACF), the rotational velocity autocorrelation function (RVACF), and the positional autocorrelation function of the fluctuating Brownian particles were calculated in some simple situations for which analytical solutions were obtained. We compared our numerical results with the analytical solutions and found excellent agreement between them, particularly in the long-time region $t > \tau_B$, while some discrepancies were found in the short-time region $t < \tau_B$. This occurs because our model is designed to simulate correct long-time behaviors of Brownian particles in host fluids.

In **Chapter 5**, the short-time motion of Brownian particles in an incompressible Newtonian

fluid under shear was examined by using a modified SPM in which external forces are introduced to approximately form a simple shear flow throughout the entire system with periodic boundary conditions. The validity of the method was carefully examined by comparing the present numerical results for the MSD with the hydrodynamic analytical solution of the GLE of a single Brownian particle in a simple shear flow. In the present study, we sought to modify the original SPM by incorporating thermal fluctuations, so that the modified SPM is valid for $\tau_B < t$, while other computational methods such as Brownian dynamics and ASD, which are based on the LE (which ignores memory effects due to fluid motions), are valid only for $\tau_B \ll \tau_D < t$. Simulations were then performed for monodisperse dispersions of repulsive spherical particles at volume fractions ranging from $\Phi = 0.002$-$0.40$. We found that the MSD in the vorticity direction grows rapidly with time and with increasing particle volume fraction. At a strain $\dot{\gamma}t \sim O(1)$, the diffusive region is attained for $\Phi \geq 0.2$. The onset of the diffusive region shifts to shorter times at higher volume fractions. The diffusion coefficient in the vorticity direction was determined from the long-time behavior of the MSD.

In **Chapter 6**, flowing concentrated dispersions were examined by a direct numerical simulation, taking into account a shear flow and thermal fluctuations. Simulations were performed for a monodisperse dispersion of repulsive sphere particles at volume fractions ranging from $\Phi = 0.31 - 0.56$ and shear rates ranging from $\dot{\gamma} = 5 \times 10^{-5} - 0.5$. the apparent viscosity for $\Phi = 0.31$ is nearly constant when $Pe < 10$ but increases linearly when $Pe > 10$. For $\Phi \geq 0.41$, the viscosity decreases at low Peclet numbers but increases linearly after reaching a Peclet number of about 10. From the viscosity versus Peclet number curves, we can obtain both the low and high limiting viscosities, and these results are in good agreement with the Krieger-Doughty relationship. The shear-thickening behavior occurs at particle Reynolds numbers $Re_p > 1$ for all volume fractions. In the thickening regions, the viscosity is proportional to the shear rate, and its slope increases monotonically with increasing volume fraction. The apparent shear viscosity can be decomposed into several contributions. We found that all contributions to the apparent shear viscosity for the shear-thickening regions increased. The shear-thinning of the apparent shear viscosity is caused mainly by the decrease in the direct interparticle component. We found that the dynamical motion of a Brownian particle for $\Phi = 0.56$ is strongly enhanced by shear flows, as compared with that for $\Phi = 0.31$, based on the mean square displacement.

In **Chapter 7**, all of the results are summarized.

In this dissertation, the dynamics of small solid particles in a Newtonian fluid was studied. However, many of the materials used in industry are more complicated. The numerical method developed in Chapter 6 is applicable to complex materials such as charged particles in an electrolyte. Kim *et al.* proposed a numerical method based on the SPM for simulating charged colloidal dispersions as a simulator for electrohydrodynamics. The combination of this simulator and our method would make it possible to investigate the relationships between rheology and the charged particle fluctuating in an electrolyte. The code developed in this dissertation will be used as a colloidal simulator in the near future.

# Acknowledgements

I am grateful to Professor Ryoichi Yamamoto for his encouragement, support and guidance throughout my PhD course. I would like to thank Professor Ko Higashitani for his support and helpful advise. I also acknowledge Professor Masahiro Ohshima and Professor Minoru Miyahara for their insightful review on this thesis. I would like to thank Professor Hiizu Nakanishi and Associate Professor Yumino Hayase for their kind guidance and valuable advice. I would like to thank Dr. Yasuya Nakayama and Dr. Kang Kim for their helpful suggestion and useful discussion.

# List of Publications

**Chapter 2**

T. Iwashita, Y. Hayase, and H. Nakanishi, "Phase Field Model for Dynamics of Sweeping Interface", J. Phys. Soc. Jpn. **74**, 1657 (2005).

**Chapter 3**

T. Iwashita, Y. Nakayama, and R. Yamamoto, "A numerical model for Brownian particles fluctuating in incompressible fluids", J. Phys. Soc. Jpn. **77**, 074007, (2008).

**Chapter 4**

T. Iwashita, Y. Nakayama, and R. Yamamoto, "Velocity autocorrelation function of fluctuating particles in incompressible fluids, -Toward direct numerical simulation of particle dispersions-", Progress of Theoretical Physics Supplement, **in press**.

**Chapter 5**

T. Iwashita and R. Yamamoto, "Short-time motion of Brownian particles in a shear flow", Phys. Rev. E, **submitted**.

**Chapter 6**

T. Iwashita and R. Yamamoto , "Direct numerical simulations for non-Newtonian rheology of concentrated particle dispersions", **to be submitted**.